Title
Design, Analysis, and Testing of Large Scale Kinetic Energy Storage Systems

Author
Xin, Siyuan

Publication Date
2015

Peer reviewed|Thesis/dissertation

Design, Analysis, and Testing of Large Scale Kinetic Energy Storage Systems

By

Siyuan Xin

A dissertation submitted in partial satisfaction of the

requirements for the degree of

Doctor of Philosophy

in

Engineering – Mechanical Engineering

in the

Graduate Division

of the

University of California, Berkeley

Committee in charge:

Professor David Steigmann, Chair

Professor Hari Dharan

Professor Paulo Monteiro

Fall 2015

Design, Analysis, and Testing of Large Capacity Kinetic Energy Storage Systems

By

Siyuan Xin

Abstract

Design, Analysis, and Testing of Large Capacity Kinetic Energy Storage Systems

by

Siyuan Xin

Doctor of Philosophy in Engineering – Mechanical Engineering

University of California, Berkeley

Professor David Steigmann, Chair

Global warming, climate change and pollution caused by the traditional energy generation technologies have become some of the biggest threats in today's world. And the need for more energy is ever increasing. Development of renewable energy, such as solar and wind, as well as distributed smart grids are needed to replace the old energy production methods. Governments have set goals of increasing the proportion of clean energy generation. One major limiting factor of the development of renewable energy is that these energy sources is not as reliable and as stable as the traditional power sources to meet the energy demand. This problem can only be effectively solved by the use of energy storage to store excess power produced by the renewable energy sources. Therefore, energy storage, especially large scale energy storage systems, will be the key factor for enabling renewable energy to become the primary sources of energy. Current energy storage technologies include batteries, flywheel, supercapacitors, pumped hydro, and so on. But due to the issues of capacity, efficiency, life cycles or costs of these current energy storage technologies, a large scale energy storage system that has low cost, long life cycles and high efficiency is yet to be developed to be integrated with renewable energy generation and smart grids. In this work, the design, analysis and tests of large scale flywheel energy storage systems are carried out. The flywheel energy storage system will feature a large steel rotor. Theoretical analysis of the stress distribution of the rotor is discussed to give a parametric view of the key elements in the design. Material testing such as tensile tests, fracture toughness tests, and fatigue crack propagation tests are conducted to characterize the behavior of the rotor material. Finite element method is used to analyze the stress-strain distribution of the rotor in order to optimize the shape of the rotor and determine the rotational speed. Also frequency analysis using finite element method gives the dynamic response of the rotor. Catastrophic failure of the rotor can cause big damages and need to be prevented from happening. And therefore, fracture mechanics is applied to analyze the safety margin and estimate the lifetime of the flywheel system. Post failure analysis is also discussed in case of rotor failure. Energy storage efficiency is a crucial factor in order for the flywheel energy storage system to be applicable. The rotor is kept in low vacuum pressure to minimize aerodynamic drag and improve energy storage efficiency. An analytical model of aerodynamic drag on the rotor is developed. Experimental measurements of drag power loss on a disc rotor inside a controlled vacuum chamber are compared to the predicted results of the analytical model. Design of sub-systems such as bearings and vacuum system are discussed at the end.

Dedicated to my family and friends.

Table of Contents

List of Figures

List of Tables

List of Symbols

Chapter 2:

α_r = heat conductivity in radial direction
α_θ = heat conductivity in hoop direction
[C] = compliance matrix
E = stored energy
E_c = energy storage capacity
E_r = elastic modulus in radial direction
E_θ = elastic modulus in hoop direction
ε = strain
ε_r = strain in radial directoin
ε_θ = strain in hoop direction
$G_{\theta r}$ = shear modulus
$\gamma_{r\theta}$ = engineering shear strain
h = height of rotor
I = moment of inertia
J = polar moment of inertia
ω = angular velocity
$\overline{\Omega}$ = angular velocity about gyroscopic axis
m = mass
$\overline{M_g}$ = gyroscopic moment
$\nu_{\theta r}$ = Poisson's ratio
r = radius
R = radius of rotor
ρ = density
[S] = stiffness matrix
σ = stress
σ_p = principal stress
σ_r = radial stress
σ_θ = hoop stress
σ_v = von Mises stress
$\tau_{r\theta}$ = torsional stress
T = temperature [K]
v_t = tip speed

Chapter 3:

e = energy density [kWh/kg]
E_{cr} = elastic modulus of composite rotor in radial direction
$E_{c\theta}$ = elastic modulus of composite rotor in hoop direction
E_{cz} = elastic modulus of composite rotor in axial direction
ν = Poisson's ratio
S_y = yield strength
V = rotor volume

Chapter 4:

a = crack characterizating length
Δ = displacement
$J = J -$ integral
K_I = mode I stress intensity factor
K_{II} = mode II stress intensity factor
K_{III} = mode III stress intensity factor
N = number of cycles
P = applied force
PE = potential energy per unit increase in crack area in a nonlinear solid
P_Q = critical load
R_s = stress ratio
U_s = strain energy stored in body
WD = work done

Chapter 5:

α' = safety factor against burst
α'' = depth of charge and discharge
α''' = ratio between weight of rotor and weight of entire flywheel enegy storage
ε_e^p = equivalent plastic strain
ε^p = plastic strain
K = shape factor of flywheel
ξ = speed factor of flywheel

Chapter 6:

A = cross section area of penetrator
a_c = critical crack length
a_i = initial crack length
c = speed of ultrasonic wave
D = penetration distance [ft]
d_o = minimal detectable flaw size
f = frequency of ultrasonic wave
K = stress intensity factor
K_{Ic} = critical stress intensity factor

K_{JIc} = critical stress intensity factor converted from J_{Ic}
L_n = length of penetrator nose
λ = wavelength of ultrasonic wave
N = nose performance coefficient
V = impact velocity [ft/s]
W = weight of penetrator [lbs]

Chapter 7:
C_d = drag coefficient
D = drag force
L = charactoerizing length
M = drag moment
μ = dynamic viscosity
ν = kinematic viscosity
P = pressure
P_{drag} = power loss due to drag
R_{air} = gas constant for air
Re = Reynold's number
Re_t = transition Reynold's number
r_t = ransition radius between laminar and turulent flow

Chapter 8:
A_1 = reliability factor for bearing life calculation
A_2 = life modifying factor for bearing life calculation
A_3 = applicaton factor for bearing life calculatoin
C = dynamic load rating
c = concentration of solution
L_{10} = bearing fatigue life for 90% survival rate
P = equivalent radial load
q = outgassing rate
R = radial load
S = pump speed
T = thrust load
V = air volume inside vaccum chamber
X = radial load factor relating to contact angle
Y = axial load

Acknowledgement

My PhD study has been a unique experience but also a difficult journey. I have many ups and downs throughout the years. Now it's time to summarize the experience. I would like to express my great gratitude to my PhD supervisor Professor Hari Dharan for providing me the opportunity and guidance. It has been a tremendous learning experience. Not only I gained knowledge and expertise, but also I have a more complete and mature view of life and world around. I won't accomplish what I have without Professor Dharan's mentorship for which I really appreciate. I also want to thank Professor David Steigmann and Professor Paulo Monteiro to be on my dissertation committee and their support.

Looking back at myself when I was an international student at University of Michigan, all I wanted after graduation is to find a job in the US. But I was not able to because nearly no company in my field would hire international students at the time. Therefore, I did what all the other international students did that was to apply for graduate school. Very fortunately I was admitted by UC Berkeley. I had an internship with GE Aviation to participate in the design of Leap-X engine for COMAC C919 aircraft. During the internship, I worked with many great engineers who are really the leading experts in their fields. I started to ask myself "what kind of person do I want to become?" I realized I had been following what most people think is right to do and what I was told to do. What I want is to become one of the best in the field of my interest and be accountable to others in a team. This is why I decided to pursue a PhD degree to be good at something. I set the goal for myself that I want to be fundamentally sound, gain the ability of learning new knowledge and have good communication skills after my PhD study.

Studying at UC Berkeley is one of the most fortunate thing in my life. It is a wonderful place not only for the smart and interesting people and great academic environment there but also for the dynamic culture and the platform it provides me to develop myself. Here I had the opportunities to learn from the smartest minds and world experts. My first supervisor is Professor Robert Ritchie. In his lab, I had the opportunity to work on characterizing the most advanced ceramic matrix composite materials for next generation aircraft engine applications with the most cutting edge equipment at Lawrence Berkeley National Lab. It has been a very fun experience to work with Dr. Hrishikesh Bale who also gave me guidance and taught me a lot of valuable knowledge. I admire Professor Ritchie not only because he is the best at what he does but also his attitude towards work. In my memory, he never stops working and truly love his work which I think is the most valuable lesson I learned from Professor Ritchie. Although the funding situation did not work out for me. I would like to thank Professor Ritchie for giving me the opportunity to learn from him and seeing the potential in me, and I am always proud of being his student.

It has been a unique journey thanks to Professor Dharan. I really appreciate his trust in me and offering me to work on flywheel energy storage. I have learned so much from this experience. I will forever remember the fun days when we worked together to design the energy storage system on paper and doing hand calculations and the crazy days and nights when we started working at 5am in the morning and doing tests until 6am next morning. I have grown from a naïve student to a person who can take on real challenges and responsibilities. During this experience, I learned very valuable knowledge on every aspect of mechanical engineering and design and developed the

ability to learn new knowledge quickly. Professor Dharan is one of the smartest person I have met. He always has dozens of new ideas and can think of things others cannot think of and at the same time gives very practical advice. He taught me to have high standard of whatever I do and also think outside of the box. I am very proud to work at Quantum Energy Storage where we have accomplished to bring a concept to a real product. I have developed great friendships with the people I work with.

The four and half years of PhD studied has helped me to forge my own view of life and the world. Exposed to the dynamic culture in the bay area and also communicating with interesting people, I started to know what I really value, what I want in life and also I learned about myself better. It is very interesting to see the changes in myself. To some extent, my PhD study is a life lesson for me to help me prepare for the future yet to come. I will continue to be a student of life and to develop my knowledge about the world.

Finally, I want to thank my family for the support they gave me. Through cheers and tears these years, my family have always provided me their care and support. With them behind me I feel strong to take on whatever challenges. As diversity introduces a man to himself, it also introduces a man to the love of family. I feel truly blessed to have my family. Also I want to thank my friends who always care about me and encourage each other to improve.

With all these being said, I am very happy to draw an end to my PhD study and welcome the new start.

Go Bears!

Siyuan Xin

12/1/2015

1. Introduction

1.1 Current Electric Grid Outlook and Drawbacks.

The need for more energy is ever increasing due to the development of households and industries. The worldwide demand for electricity is projected to double by 2050. [1] Meanwhile the conventional electric grid and power generation methods are not efficient and cause problems such as pollution and global warming. Currently, the electric power infrastructure generates and outputs power to match the load demand. Without a store energy system, the infrastructure must supply sufficient power capacity to the grid to meet peak demand requirements. However, during most of the time, the load demand is below peak and the capacity of power generation is wasted. On the other hand, the transmission and distribution system must also be sized to be able to satisfy power transfer requirements for the peak demand, and the transmission capacity is also wasted most of the time. Furthermore, since the demand changes frequently, to match the demand power generation is also continuously ramped up and down. The cyclic demand and supply reduce the efficiency of power plants, which results in higher fuel consumption and higher emissions per energy generated. To solve these problems, renewable energy sources are needed to become the primary energy source. However, these energy sources such as solar and wind do not deliver an adjustable regular power supply. They rely on the weather and climate to work effectively. Electricity generated from renewable sources can rarely provide immediate response to meet the consumption needs. In order for these new sources to become reliable and stable as the primary sources of energy, energy storage is a key factor that is currently missing in the power infrastructure. [2]

1.2 The Role of Energy Storage

Potential applications of energy storage on the electric grid include frequency regulation and load following where instantaneous responses are desired, as well as peak shaving and load shifting where capacity and efficiency of the energy storage are important. Another application of energy storage is for power conditioning and uninterrupted power supply (UPS). All these applications will enable the grid to be more reliable and stable. Among the applications, load shifting has more potential market because of the benefit in storing the excess energy and releasing it at when power generation is less than the demand. [3] Energy storage helps to decouple power generation and load demand, which simplify the overall power generation and transmission system of the electric grid. Several applications of energy storage integrated with renewable energy sources and electric grid demonstrates its value of providing reliability of the renewable energy generation [4]

1.3 Types of Energy Storage

Current energy storage technologies include batteries, supercapacitors, flywheels, compressed air, pumped hydro, and etc. For large-scale applications, the existing energy storage technologies can be divided into four categories: mechanical, electrical, chemical, and electrochemical. [5] An overview of the existing types of energy storage technologies, their applications and limitations are discussed in [6-11]. However, existing energy storage solutions are very expensive that it has not been cost-effective to be integrated with power generation and transmission system to provide the economic factor of serving the peak load and sufficient operating margin to meet consumer demands for reliability. [1]

1.4 Flywheel Energy Storage Background

Flywheel has been used for hundreds of years to storage energy. [12] A flywheel is a rotor rotating about an axis, which stores energy in the form of kinetic energy. Electric power is transformed to kinetic energy of the flywheel by an electric motor which accelerate the rotation of the flywheel. The amount of energy that can be stored in the flywheel depends on its angular velocity and the moment of inertia. The faster the flywheel rotates the more energy it stores. On the other hand, the electric motor retrieve the kinetic energy to electric power as a generator by applying a decelerating torque to the flywheel. Recent development of flywheel energy storage has demonstrated its potential to be integrated with clean energy source and electric grid. However, most of the current systems are developed for frequency regulation and UPS applications. They typically feature fiber reinforced composite rotors built with magnetic bearings. [13-14] A low-cost large scale flywheel energy storage system is yet to be developed for a broader range of applications such as load shifting.

1.5 Advantages and Disadvantages of Flywheel Energy Storage

The advantages of flywheel energy storage systems include:

- High charge and discharge rates (high power density): The charge and discharge rates of the flywheel energy storage depends on the power rating of the electric motor. With design of high power electric motor and robust transmission between the motor and the flywheel, the flywheel system can store or release energy at a very high rate.
- High efficiency: The flywheel energy storage system can have high efficiency if the sub-systems are proper designed. To reduce drag power loss, flywheels are usually kept in a vacuum chamber. The energy storage efficiency is typically around 90%. [10]
- No capacity degradation: Unlike a chemical energy storage such as batteries, flywheel energy storage has no capacity degradation since the mechanical properties of the rotor material remain the same.
- Long lifetime of the flywheel: The lifetime of a flywheel depends on the material properties of the rotor as well as the cyclic load. The rotor is usually designed to operate at a maximum speed at which the stress level is much smaller than the yield strength of the material. The fatigue life of the rotor is typically over 20 years.
- Fast response time: The fast response of flywheel energy storage system time typically in milliseconds makes them ideal for frequency regulation and load following.
- Measurable state of charge: The state of charge of the flywheel energy storage system can be measured by the rotational speed of the rotor which is measured by the sensor in electric motor.
- Environmental friendly, low environmental impact: The materials used in a flywheel energy storage system, such as steel, carbon composites, aluminum and etc., are environmental friendly and recyclable, which is a major advantage over batteries.

The main disadvantage of flywheel energy storage is the standby loss. Since flywheel energy storage is a rotational machinery, the frictional power loss of the bearings and vacuum seals will always present when the flywheel is spinning. Also electric motor can also have power loss. The power loss can be reduced or eliminated by proper design of the sub-systems.

1.6 Challenges of the Technology

Developing a large scale flywheel energy storage that can solve the problems of the current electric grid faces the following three challenges: 1) reducing standby loss; 2) being cost effective; 3) preventing catastrophic failure of rotor. For applications such as load shifting, the energy storage are sometimes required to hold energy for a long period of time. Therefore, reducing standby loss will improve the roundtrip efficiency of the energy storage system. The system needs to be cost effective to be integrated into the entire electric grid. Many of the existing flywheel energy storage systems use composite rotors and magnetic bearings. The high production cost for these components has kept flywheel energy storage from grid applications. Safety is always a major concern. Catastrophic failure of the rotor can cause massive damages which need to be prevented by the design. All these three challenges are addressed in this dissertation.

1.7 Scope of Work

In this dissertation, design, analysis and tests of a low-cost large scale flywheel energy storage system are carried out. The flywheel energy storage will feature a large steel rotor. Theoretical analysis of the stress distribution of the rotor is discussed to give a parametric view of the key elements of the design. Mechanical tests on the rotor material such as tensile tests, fracture toughness tests, and fatigue crack propagation tests are conducted to characterize the behavior of the rotor material. Finite element method is used to analyze the stress-strain distribution of the rotor in order to optimize the shape of the rotor and determine the rotational speed. Also frequency analysis using finite element method gives the dynamic response (resonant modes and frequencies) of the rotor. Catastrophic failure of the rotor can cause damaging consequences and need to be prevented from happening. And therefore, fracture mechanics is applied to analyze the safety margin and estimate the lifetime of the rotor. Post failure analysis is also discussed in case of a rotor failure. Energy storage efficiency is a crucial factor for this flywheel system to be applicable. To improve energy storage efficiency, the rotor is kept in low vacuum pressure to minimize aerodynamic drag. An analytical model of aerodynamic drag on the rotor is developed. Experimental measurements of drag power loss on a rotating disc rotor are compared to the prediction of the analytical model. Design of sub-systems are discussed at the end which covers the design and analysis of the bearings and vacuum system. This flywheel energy storage system has the potential to solve the reliability and stability problem of the renewable energy sources and be cost effective to be integrated with the electrical grid.

2. Rotor Mechanics and Kinematics

Flywheel electric energy storage systems consist of a rotor with a shaft that spins rapidly within a robust enclosure. Electric power is converted to kinetic energy by an electric motor and stored in the form of the angular rotational energy of the rotor. The amount of energy storage capacity is determined by the geometry, material and rotational speed of the rotor. To calculate the stored energy, one can integrate the kinetic energy of infinitesimal volumes of a complex shaped the rotor:

$$E = \int_V \frac{1}{2}\rho\omega^2 r^2 dV \tag{2.1}$$

As the rotor is spinning, the material is seeing radial and hoop stress caused by the rotational body force of the rotor mass as well as the torsional stress caused by the torque applied by the motor. The force on the rotor in the axial direction is often low compared to the other forces. Within the elastic regime of the material, the stress-strain relation is described by generalized Hooke's Law:

$$\sigma_i = C_{ij}\varepsilon_j \tag{2.2}$$

Where σ_i are the stress components, ε_j are the strain components, and C_{ij} is the stiffness matrix.

$$[\sigma_j] = \begin{bmatrix} \sigma_1 \\ \sigma_2 \\ \sigma_3 \\ \tau_{23} \\ \tau_{31} \\ \tau_{12} \end{bmatrix} \qquad [\varepsilon_i] = \begin{bmatrix} \varepsilon_1 \\ \varepsilon_2 \\ \varepsilon_3 \\ \gamma_{23} \\ \gamma_{31} \\ \gamma_{12} \end{bmatrix} \tag{2.3}$$

This constitutive law can be rewritten in the form of the compliance matrix S_{ij}, where the compliance matrix is the inverse of the stiffness matrix $[S] = [C]^{-1}$.

$$\varepsilon_i = S_{ij}\sigma_j \tag{2.4}$$

$$[S] = \begin{bmatrix} S_{11} & S_{12} & S_{13} & S_{14} & S_{15} & S_{16} \\ S_{12} & S_{22} & S_{23} & S_{24} & S_{25} & S_{26} \\ S_{13} & S_{23} & S_{33} & S_{34} & S_{35} & S_{36} \\ S_{14} & S_{24} & S_{34} & S_{44} & S_{45} & S_{46} \\ S_{15} & S_{25} & S_{35} & S_{45} & S_{55} & S_{56} \\ S_{16} & S_{26} & S_{36} & S_{46} & S_{56} & S_{66} \end{bmatrix} \tag{2.5}$$

If the rotor is axial symmetric and conditions of plane stress can be satisfied, the stress in the rotor is only a function of radius r. The constitutive law of the rotor material can be written as:

$$\begin{bmatrix} \varepsilon_\theta \\ \varepsilon_r \\ \gamma_{r\theta} \end{bmatrix} = [S]\begin{bmatrix} \sigma_\theta \\ \sigma_r \\ \tau_{r\theta} \end{bmatrix} + T\begin{bmatrix} \alpha_\theta \\ \alpha_r \\ 0 \end{bmatrix} = \begin{bmatrix} 1/E_\theta & -\nu_{\theta r}/E_\theta & 0 \\ -\nu_{\theta r}/E_\theta & 1/E_r & 0 \\ 0 & 0 & 1/G_{\theta r} \end{bmatrix}\begin{bmatrix} \sigma_\theta \\ \sigma_r \\ \tau_{r\theta} \end{bmatrix} + T\begin{bmatrix} \alpha_\theta \\ \alpha_r \\ 0 \end{bmatrix} \tag{2.6}$$

The strain compatibility relation between hoop stress σ_h and radial stress σ_r is expressed by:

$$\frac{d(\sigma_r r h)}{dr} - \sigma_\theta h + \rho\omega^2 r^2 h = 0 \tag{2.7}$$

By plugging the strain compatibility relation into the constitutive law, the following second-order differential equation of radial stress can be achieved:

$$\frac{d^2\sigma_r}{dr^2} + \frac{d\sigma_r}{dr}\left(\frac{3}{r} + \frac{1}{h}\frac{dh}{dr}\right) + \sigma_r\left[\frac{1}{r^2}\left(1 - \frac{E_\theta}{E_r}\right) + \frac{1}{r}(2 + \nu_{\theta r})\frac{1}{h}\frac{dh}{dr} + \frac{d}{dr}\left(\frac{1}{h}\frac{dh}{dr}\right)\right] + \rho\omega^2(3 + \nu_{\theta r}) + E_\theta\alpha_\theta\left[\frac{T}{r^2}\left(1 - \frac{\alpha_r}{\alpha_\theta}\right) + \frac{1}{r}\frac{dT}{dr}\right] = 0 \tag{2.8}$$

2.1 Solid Disc Steel Rotor

A solid thin disc steel rotor is a simplified case of the rotor design which provides a parametric analysis of the rotor kinematics. For a solid disk rotor with radius R, the energy stored is given by the following equation.

$$E = \frac{1}{2}I\omega^2 = \frac{1}{4}mv_t^2 \tag{2.9}$$

where E is kinetic energy stored in the flywheel, I is moment of inertia and ω is the angular velocity of the flywheel. The moment of inertia for any object is a function of its shape and mass. For steel rotors the dominant shape is a solid cylinder giving the following expression for I:

$$I = \frac{1}{2}mR^2 = \frac{1}{2}\pi\rho h R^4 \tag{2.10}$$

Since the rotor is made out of isotropic material in this case, the above second order differential equation can be simplified as:

$$\frac{d^2\sigma_r}{dr^2} + \frac{d\sigma_r}{dr}\left(\frac{3}{r} + \frac{1}{h}\frac{dh}{dr}\right) + \sigma_r\left[\left(\frac{2+\nu}{r}\right)\frac{1}{h}\frac{dh}{dr} + \frac{d}{dr}\left(\frac{1}{h}\frac{dh}{dr}\right)\right] + \rho\omega^2(3+\nu) + \frac{E\alpha}{r}\frac{dT}{dr} = 0 \tag{2.11}$$

Furthermore, for a disc rotor with constant thickness, the equation can be reduced to:

$$\frac{d^2\sigma_r}{dr^2} + \frac{3}{r}\frac{d\sigma_r}{dr} + \rho\omega^2(3+\nu) + \frac{E\alpha}{r}\frac{dT}{dr} = 0 \tag{2.12}$$

Assuming no thermal effects are present. The radial stress and hoop stress are functions of the distance r from the location to the rotational axis which can be obtained by solving the differential equation above with proper boundary conditions.

$$\sigma_r(r) = \frac{3+\nu}{8}\rho\omega^2 R^2\left(1 - \frac{r^2}{R^2}\right) \tag{2.13}$$

$$\sigma_\theta(r) = \frac{3+\nu}{8}\rho\omega^2 R^2\left(1 - \frac{1+3\nu}{3+\nu}\cdot\frac{r^2}{R^2}\right) \tag{2.14}$$

Torque applied by the motor also induces torsional stress τ which can be calculated by:

$$\tau = \frac{Tr}{J} \tag{2.15}$$

The maximum values for both radial and hoop stress appears at the center of the rotor where r equals 0 is given by:

$$\sigma_{r_{max}} = \sigma_{\theta_{max}} = \frac{3+\nu}{8}\rho\omega^2 R^2 \tag{2.16}$$

To determine if the rotor is safe to spin at a certain rotational speed, one can compare the maximum stress with the maximum principal stress or the Von Mises Stress depend on the material behavior. When the material is brittle, for example carbon fiber reinforced composites, maximum principal stress is applicable as the failure criterion. Meanwhile, for ductile materials such as steel, the Von Mises stress is often used as the yield criterion. For a disk rotor under plane stress,

$$\sigma_p = \frac{\sigma_r + \sigma_\theta}{2} \pm \sqrt{\left(\frac{\sigma_r - \sigma_\theta}{2}\right)^2 + \tau^2} \tag{2.17}$$

$$\sigma_v = \sqrt{\frac{(\sigma_r - \sigma_\theta)^2 + (\sigma_\theta - \sigma_z)^2 + (\sigma_z - \sigma_r)^2 + 6\left(\tau_{\theta z}^2 + \tau_{zr}^2 + \tau_{r\theta}^2\right)}{2}} \tag{2.18}$$

$$\sigma_v = \sqrt{\frac{(\sigma_r - \sigma_\theta)^2 + \sigma_\theta{}^2 + \sigma_r{}^2 + 6\tau^2}{2}} \tag{2.19}$$

As ωR equals v_t, the tip speed, the maximum stress caused by rotation is a function of tip speed of the rotor. For a disk rotor, the maximum stresses are proportional to square of tip speed if the material is in the elastic regime. And the equation of maximum stress can be simply written as:

$$\sigma_{r_{max}} = \sigma_{\theta_{max}} = \frac{3+\nu}{8}\rho v_t^2 \propto v_t^2 \tag{2.20}$$

This relation between the maximum stress and tip speed is used to represent other complex shaped rotors, and is a guiding rule for designing the geometry and speed of the rotor. More accurate calculation of the stress and strain distribution of complex shaped rotors is achieved by finite element analysis which will be shown in later chapters.

2.2 Gyroscopic Moment of a Flywheel

A flywheel spinning about a principal axis of inertia with angular velocity $\bar{\omega}$ will react with a gyroscopic moment when its axis of rotation moves with an angular velocity $\bar{\Omega}$. The gyroscopic moment is given by

$$\overline{M_g} = J\bar{\omega} \times \bar{\Omega} \tag{2.21}$$

Where J is the moment of inertia of the flywheel about its axis of spin.

The gyroscopic moment due to the earth's precession can create radial forces on the shafts of the flywheel acting on the bearings. In order to design a safe bearing system, the maximum gyroscopic moment need to be calculated at the maximum speed of the flywheel. And therefore, it can be related to the energy storage capacity of the flywheel system E_c.

$$\bar{M} = \frac{2E_c}{\alpha''\omega}\frac{\bar{\omega}}{\omega} \times \bar{\Omega} \tag{2.22}$$

where α'' is the depth of charge and discharge factor of the energy storage system which is the ratio between the minimal energy and maximum energy in the system.

The radial forces on the bearings can be calculated from the earth's precession moment on the rotor. The magnitude of the forces depend on the spacing between the bearings and the bearing configuration.

3. Rotor Material Selection

As shown in the previous chapter, the two important factors in the calculation of the energy, mass and speed are related to material properties such as density and yielding strength, if we define the volumetric energy density of the flywheel to be the stored energy per unit volume. Here we assume the rotor is disk shaped and made of a homogeneous isotropic material. The equation of the stored energy for the rotor can be re-written as shown below. The energy density for the flywheel is determined by the material properties of the rotor. For a disk rotor, the energy density e (kwh/kg) is only related to the yielding strength and Poisson's ratio of the material.

$$E = \frac{2V\sigma_{r_{max}}}{3+\nu} \tag{3.1}$$

$$e = \frac{E}{m} = \frac{2\sigma_{r_{max}}}{(3+\nu)\rho} \propto \frac{S_y}{(3+\nu)\rho} \tag{3.2}$$

Two kinds of commonly used material for flywheels are steel and carbon composites. Compact steel flywheels have been implemented in vehicle powertrains to keep the engine operating at a relative constant speed instead of turning kinetic energy of the vehicle into wasted heat on the brakes. Meanwhile, several research labs and companies, such as US Flywheel Systems and Beacon Power, have demonstrated the applications of energy storage systems using fiber reinforced composite flywheels. [13]

Steel rotors are capable of storing a large amount of energy due to the high density of steel. They have the potential to be used for utility scale energy storage. In addition, steel can be made to be strong which means having a high fracture toughness by alloying and heat treatments, and thus steel rotors can have more tolerance of defects and impurity and therefore a long life time. However, due to the large weight of steel rotors, designing the sub-systems around the rotors is pushing the limits of many of the current technologies, and large scale flywheel energy storage system with steel rotors remain a design challenge.

Composite rotors on the other hand generally are made of fiber reinforced composites that have high tensile strength. The usual choices of the fiber materials for composite material flywheels are glass fiber, carbon or aramid fiber, better known as Kevlar. Therefore, composite rotors can rotate at very high speed. Also, due to the high tensile strength, composite rotors can have higher energy density. For applications where space is limited such as residential energy storage and automobiles, composite rotors are preferable. Currently composite rotors can be seen in many Uninterrupted Power Supply (UPS) applications where large amount of energy storage is not required.

3.1 Material Properties

Table 3.1 presents the material properties of commonly used materials for flywheel fabrication. As shown in Equation 3.2, energy density of the flywheel energy storage is related to the tensile strength of the material as well as the Poisson's ratio. Carbon fiber reinforced composite rotors can have higher tensile strength than steel rotors, and therefore composite flywheels usually have higher energy density than steel flywheels. Table 3.2 gives a comparison of the energy density of several energy storage methods.

Rotor Material	Density (kg/m^3)	Tensile Strength (MPa)	Cost ($\$/kg$)
AISI 4340 Steel	7800	1400	1
E glass fiber/polymer	1940	100	11.0
S glass fiber/polymer	1800	1470	24.6
HS carbon fiber/polymer	1520	1950	101.8
HM carbon fiber/polymer	1510	1650	31.3
Kevlar 49 fiber/polymer	1420	1400	20.0

Table 3.1: Material properties of common rotor materials. [15]

Energy Storage	Energy Density (Wh/kg)
Lithium-ion battery	80 - 200
Lead acid	30 - 50
Flywheel	5 - 100
Flow battery	20 - 90
Compressed air	3.2 - 5.5

Table 3.2: Energy density comparison of several types of energy storage. [16-17]

For electric grid scale applications, one of the most important parameters for energy storage is the ratio between energy density and unit cost which yields energy per dollar. It measures the cost effective of the system. In this case, steel rotors have the advantage of cost effectiveness over composite rotors.

3.2 Mechanics of Rotor Materials

Steel demonstrates isotropic behavior although its microscopic structure is non-homogeneous. On the other hand, composite rotors are usually made of circumferentially oriented fiber reinforced composite laminates which have orthotropic behavior. In terms of mechanical analysis, the stiffness and compliance matrix of the constitutive law for isotropic material can be simplified to 2 elastic coefficients, elastic modulus E and Poisson's ratio ν.

$$[\varepsilon] = \frac{1}{E}\begin{bmatrix} 1 & -\nu & -\nu & 0 & 0 & 0 \\ -\nu & 1 & -\nu & 0 & 0 & 0 \\ -\nu & -\nu & 1 & 0 & 0 & 0 \\ 0 & 0 & 0 & 1+\nu & 0 & 0 \\ 0 & 0 & 0 & 0 & 1+\nu & 0 \\ 0 & 0 & 0 & 0 & 0 & 1+\nu \end{bmatrix}[\sigma] \tag{3.3}$$

For orthotropic materials, the stiffness matrix has 9 elastic coefficients.

$$[\varepsilon] = \begin{bmatrix} S_{11} & S_{12} & S_{13} & 0 & 0 & 0 \\ S_{12} & S_{22} & S_{23} & 0 & 0 & 0 \\ S_{13} & S_{23} & S_{33} & 0 & 0 & 0 \\ 0 & 0 & 0 & S_{44} & 0 & 0 \\ 0 & 0 & 0 & 0 & S_{55} & 0 \\ 0 & 0 & 0 & 0 & 0 & S_{66} \end{bmatrix}[\sigma] \tag{3.4}$$

where these elastic coefficients are related to the engineering constants E_1, E_2, E_3, ν_{12}, ν_{13}, ν_{23}, G_{12}, G_{13}, and G_{23} of the composite material. The engineering constants can be measured by

mechanical tests and also calculated using the rules of mixture theory from the known properties of the fiber and matrix materials.

To determine the engineering properties of a composite flywheel, we can divide the rotor into infinitesimal laminate plates shown in the Figure 3.1.

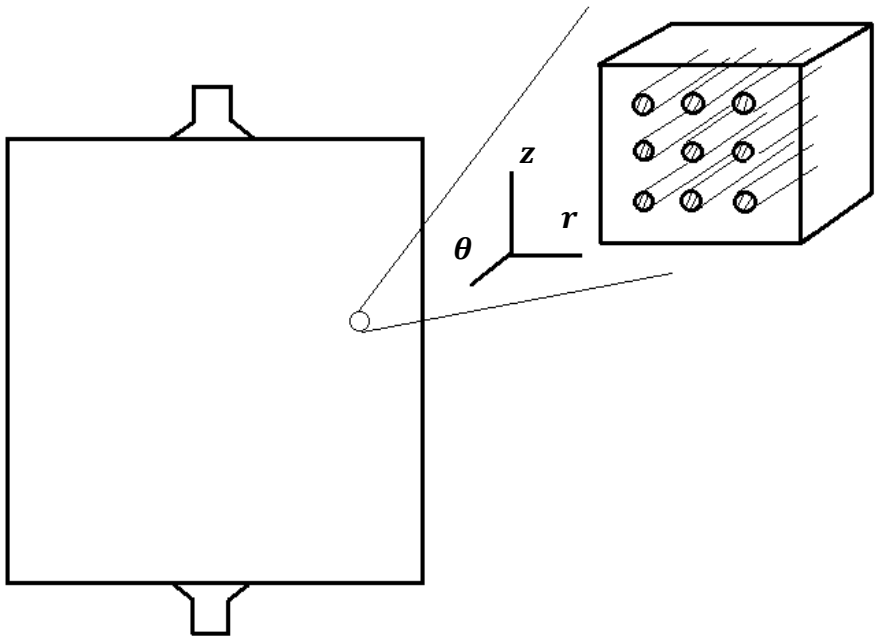

Figure 3.1 Simplified model of fiber reinforced composite rotor of flywheel energy storage.

Elastic modulus of the composite rotor in the circumferential direction $E_{c\theta}$ is function of the elastic modulus of the fiber E_f and elastic modulus of the matrix E_m in the parallel model. Elastic modulus of the composite rotor in the radial and vertical directions E_{cr} and E_{cz} is function of the elastic modulus of the fiber E_f and elastic modulus of the matrix E_m in the series model.

$$E_{c\theta} = \sum E_i v_i = E_f v_f + E_m v_m \tag{3.5}$$

$$E_{cr} = E_{cz} = \left[\sum \frac{v_i}{E_i}\right]^{-1} \tag{3.6}$$

3.3 Manufacturing Process of Rotor Materials

The manufacturing process for steel rotor starts with the casted steel ingot. The composition of the steel ingot are controlled to have the right amounts of the alloying elements in order to achieve the desired material properties though heat treatment process later. The ingot teeming are typically done by top pouring into tapered molds. Two other steel melting procedures that were developed for high quality steels are Vacuum Arc Remelting (VAR) and Electroslag Remelting (ESR). These procedures can guarantee less defects and higher purity in the steel ingot. [18] However, the cost

of VAR and ESR steel ingot is much higher. The steel ingot is then forged into forging dies to have a rough rotor geometry. Next, the forged rotor is machined to be close to the final geometry of the rotor and then sent for the heat treatment process to obtain the required mechanical properties. The heat treatment procedure is tailored corresponding to the size and shape of the rotor to achieve approximately a homogenous temperature change with in the rotor. Difference heating and cooling rate within the rotor can lead to material property variation and cracks. After heat treatment, the rotor goes through another machining process to have the desired dimensions and surface finishes. Corrosion resistant coatings may be applied to the rotor surface to protect the rotor from corrosion.

Most common material used in composite rotors is carbon fiber reinforced composites. The primary element of the composite is a carbon filament which is produced from a precursor polymer such as polyacrylonitrile (PAN). The precursor is first drawn or spun into filament yarns, using chemical and mechanical processes to initially align the polymer atoms in a way to enhance the final physical properties of the completed carbon fiber. [19] After drawing or spinning, the polymer filament yarns are then carbonized by heat to produce the final carbon fiber. The fibers are then surface treated and arranged into a mold in the shape of the rotor. The mold is filled with the matrix material usually thermosetting resin. Next, the matrix material need to be cured to result in hardened finished rotor. Many methods can be used for curing, including autoclave curing, vacuum molding (VM), resin transfer molding (RTM), resin film infusion (RFI) and etc. [20]

Compared to steel rotor manufacturing, composite rotor manufacturing process involves more steps and higher cost. For the application of a large scale energy storage system to be integrated with utility grid and clean energy farms, large steel rotors have the advantages of higher energy storage capacity, lower cost, easier manufacturing process and recyclable materials. Therefore, steel rotors will be the choice for the large scale flywheel energy storage systems in this dissertation.

4. Materials Testing

The previous chapter discussed the two categories of material, steel and carbon composites, which are commonly used for the material of the rotor in a flywheel energy storage system. For an energy storage system that can be integrated into the current electric grid system, large steel rotors have the advantages of both the capacity of storing more energy and more economic to fabricate, and thus are the better choice for this application. We will focus on characterizing steel rotors from this chapter on. Obtaining the material properties of the rotor are essential to design the geometry and rotational speed of the rotor. Critical properties that are important parameters in rotor design, such as yielding strength, ultimate tensile strength, ductility and fracture toughness, can be determined by conducting mechanical tests on testing samples of the rotor material. This chapter focuses on three mechanical tests: tensile test, fracture toughness test and fatigue crack propagation tests that were completed on samples of a steel rotor. Through these tests, mechanical properties were achieved.

4.1 Tensile Test

The purpose of the unidirectional tensile tests is to measure the elastic modulus, yield strength, tensile strength as well as elongation. These properties will be implemented into calculations and finite element analysis of the stress and strain distribution of the rotor which will lead to the determination of allowable operation speed, volume expansion and safety margins of the rotor design and also sub-system design. Tensile tests were conducted on “dog-bone” samples machined out of the rotor material block.

During the heat treatment process of a large steel rotor, rotors go through temperature cycles. The thickness of the rotor can have effects on the cooling rate of the material which leads to variance in mechanical properties of surface material and center material. Therefore, the tensile tests samples were machined out of rotor material out of both surface and center of a forged test block which had the same thickness as the rotor. The test block went through the same forging and heat treatment process as the rotor, and therefore its properties should be identical to the rotor. The orientation of the test samples has to align with the direction of the load of the rotor which is in the horizontal plane. The following Figure 4.1 shows the location and orientation of the samples in the forged test block. Test samples were taken near the surface of the test block which is representative of the material at the rotor surface. The other samples were taken from the center of the test block corresponding to a region at the interior center of the rotor.

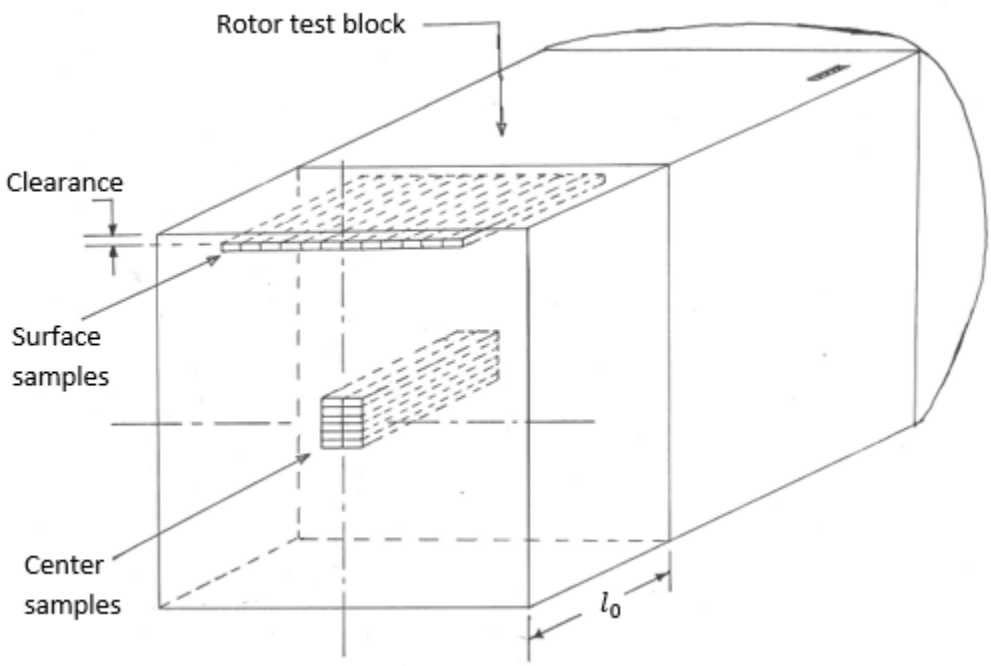

Figure 4.1: Tensile test samples machined out of a test block of rotor material.

The samples were prepared into "dog bone" shaped specimens shown in Figure 4.2 referring to the requirements in ASTM Standard E8 which describes the test methods for tension testing of metallic metals. The drawing of the tension test sample is shown in Appendix A.

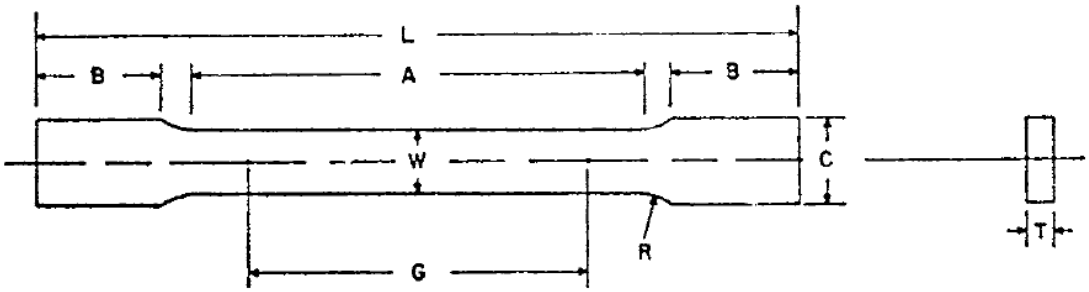

Figure 4.2: Representative drawing of tensile test sample of rotor material.

An extensometer was installed on the sample to measure the change in length of the samples to feed in strain calculation. The strain values were calculated by comparing the length measurement of the extensometer to the original gauge length of the sample. The elongation value was obtained by comparing the final measurement of the length of the gauge section to the original length. The tests were conducted under constant strain rate of 0.005 mm/mm/min. The interpreted stress-strain curves from the tensile test data are shown in Figure 4.3. Notice that these two curves do not represent the full stress-strain curve of the material samples. The extensometer only measured up to certain length, and therefore accurate strain values were measured up to the limit of the extensometer. Since the interested properties obtained from tensile tests are elastic modulus, yield

strength, ultimate tensile strength and elongation, strain measurement for the full stress-strain curve is not necessary.

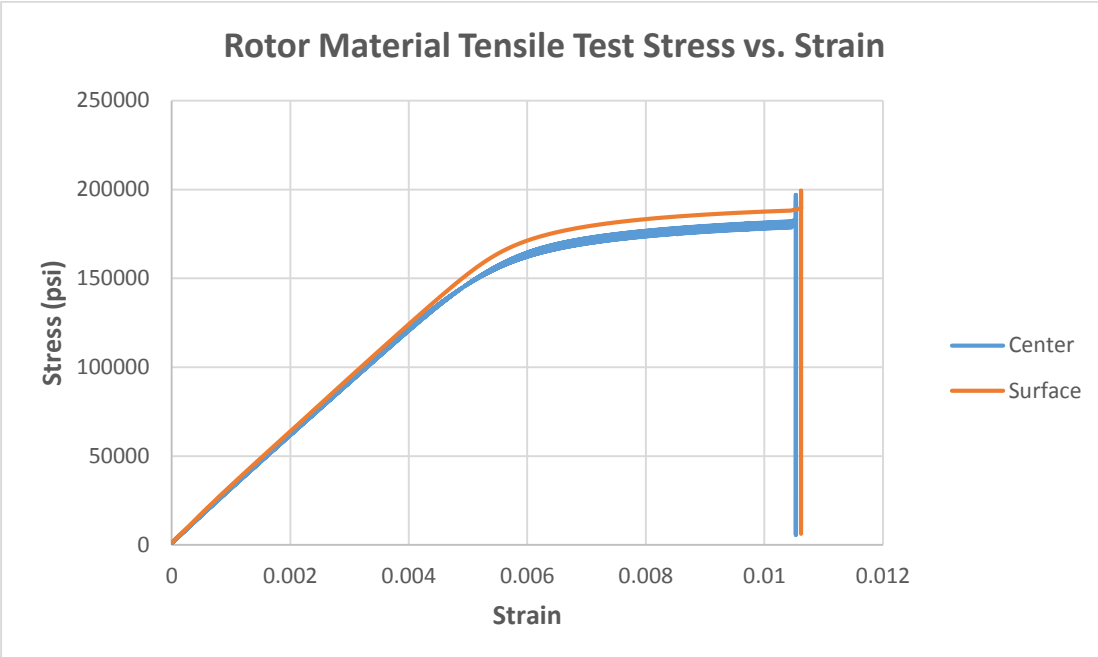

Figure 4.3: Rotor material tensile test data and results.

The average values of the measured material properties are listed in Table 4.1, where the yield strengths were interpreted according to 0.2% offset, and the elongations were calculated based on the measurements of the length of the gage section of the samples. As seen in the table, the difference of the material properties between the center material and surface material were observed. The surface material is tougher than the center material in terms of higher strengths and higher strain to failure values. These measured mechanical properties will later be the input in the finite element analysis to simulate the behavior of the rotor material.

Material Sample	Elastic Modulus (GPa)	Yield Strength (MPa)	Ultimate Tensile Strength (MPa)	Elongation or Strain to Failure (%)
Center Sample	205	1205	1347	11
Surface Sample	205	1259	1369	11.75%

Table 4.1: Measured mechanical properties of rotor material from unidirectional tensile tests.

This gradient of change in mechanical properties through the thickness of the rotor is caused by the difference in the cooling rate in the forging and heat treatment process. Since large rotors are preferable in applications of large capacity energy storage, designing the size and thickness of the rotor to ensure more homogeneity of material properties throughout the rotor remains a challenge today.

4.2 Fracture Toughness Test

No material is perfect. Flaws such as impurities, voids, micro cracks and grain boundaries induced from the raw material and in the fabrication processes exists in the rotor material. These flaws are usually where fracture starts and will cause the actual fracture toughness to be lower than the theoretical value. By obtaining the fracture toughness value and the maximum detectable defects within the rotor, one can calculate the maximum allowable rotational speed of the rotor to avoid catastrophic failure.

Fracture toughness, K_{1c}, is a measurement of material's resistance to fracture for the opening mode (Model I) loading in linear elastic fracture mechanics (LEFM). LEFM is only valid if the nonlinear material deformation is confined to a small region surrounding the crack tip. It is not applicable to materials that exhibit time-dependent, nonlinear behavior, i.e. plastic deformation, such as structural steels. [21] J-integral is used as the characterizing parameter which characterizes the local distribution of stresses, strain and displacements at a crack tip in a nonlinear elastic solid. [22]

$$J = -\left(\frac{\partial PE}{\partial A}\right) \tag{4.1}$$

where PE is the potential energy per unit increase in crack area A in a nonlinear elastic solid. PE is the difference between the strain energy stored in body U_s and work done WD.

$$PE = U_s - WD = \begin{cases} \int_0^{\Delta} P d\Delta & for\ fixed\ displcement \\ -\int_0^{P} \Delta dP & for\ fixed\ load \end{cases} \tag{4.2}$$

J-integral can be determined by laboratory measurements of the loads and displacements.

$$J = \begin{cases} -\int_0^{\Delta} \left(\frac{\partial P}{\partial A}\right)_{\Delta} d\Delta & for\ fixed\ displacement \\ \int_0^{P} \left(\frac{\partial \Delta}{\partial A}\right)_{P} dP & for\ fixed\ load \end{cases} \tag{4.3}$$

Under elastic conditions, J-integral can be related to the stress intensity factor K by:

$$J = \frac{K_I^2}{E'} + \frac{K_{II}^2}{E'} + \frac{K_{III}^2}{E'} \tag{4.4}$$

$$E' = \frac{E}{1 - \nu^2} \tag{4.5}$$

Compact tension specimens were machined out of a test block corresponding to the maximum stress locations in the rotor which experiences the highest stress in the energy storage system. The test block had similar dimensions and have gone through identical heat treatment process as the rotor. Size, configuration and preparation of the specimens satisfied the specifications in ASTM

Standard E1820-01. Figure 4.4 gives a parametric view of the geometry of a compact tension specimen. The drawing of the compact tension specimen is shown in Appendix B.

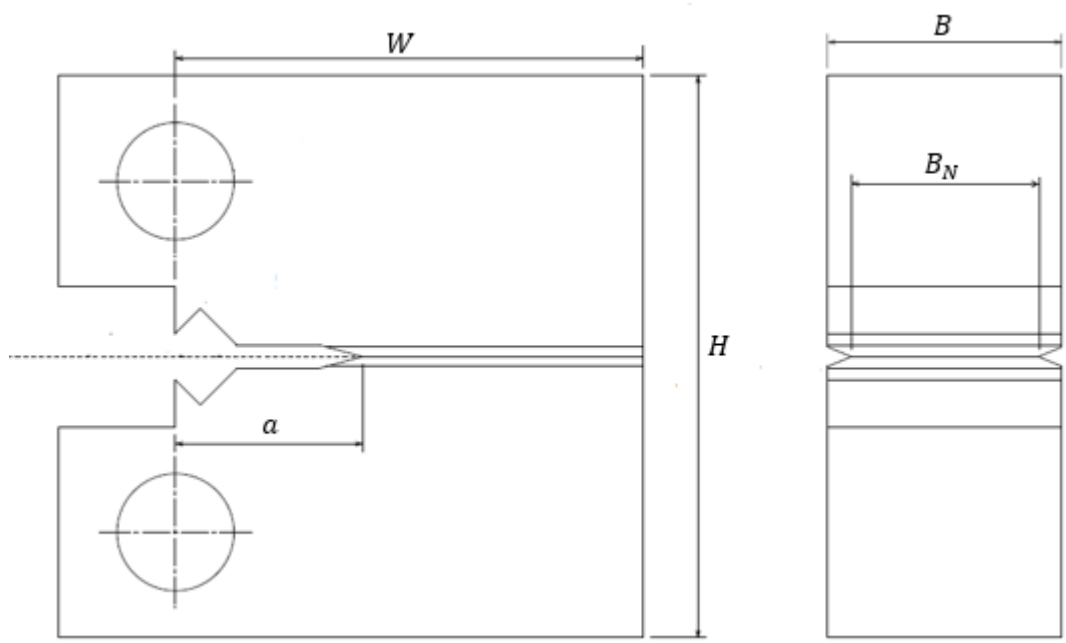

Figure 4.4: Geometry of compact tension specimen for fracture toughness test and fatigue crack propagation test.

Specimens were taken from both the surface of the test block and the center of the test block corresponding to the highest stress locations in the rotor. Loads were applied perpendicular to notches and fatigue cracks in the specimens to simulate model I fracture. Test setup is shown in Appendix B. Loading direction and crack opening of the specimens was designed to mimic the loading and potential crack opening in a spinning rotor. The testing procedure and post analysis were conducted according to ASTM Standard E1820. The specimens were pre-cracked in fatigue according to ASTM E1820 7.4.5.1, and the fatigue crack length satisfied ASTM E1820 7.4.2. J-integral measurements versus crack growth were measured in these tests and are represented in J-R curve shown in Figure 4.5 for one specimen. Fracture toughness J_{Ic} is defined near the initiation of stable crack growth. J_Q is defined as the intersection between the J-R curve and a 0.2mm offset line. J_{Ic} equals to J_Q when the specimen size requirements in ASTM E1820 A9.8 were met.

$$J_{Ic} = J_Q \tag{4.6}$$

$$when \quad B, b_o \geq \frac{20J_{max}}{\sigma_Y} \tag{4.7}$$

$$and \quad \Delta a_{max} \leq 0.25 b_o \tag{4.8}$$

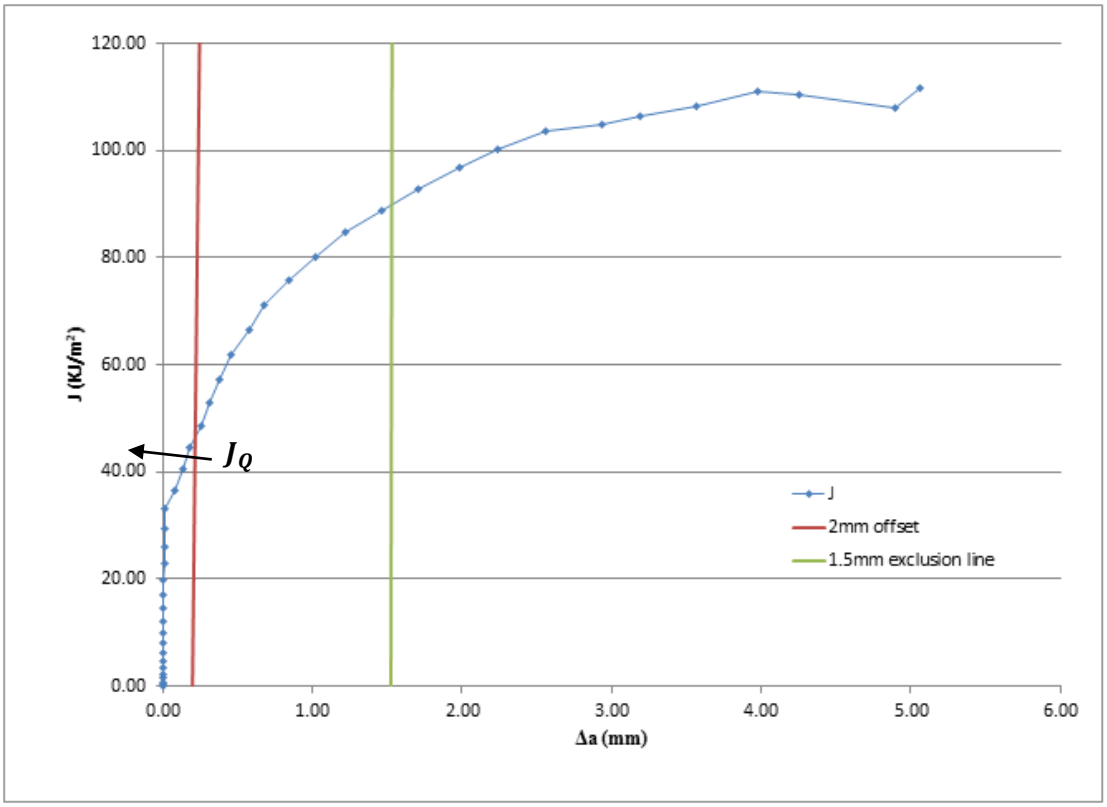

Figure 4.5: J resistance curve from fracture toughness test of a compact tension sample of rotor material.

In order to determine fracture toughness K_{Ic} in accordance with these tests, it is necessary first to calculate a conditional result, K_Q, and then to determine whether this result is consistent with size and yield strength requirements in ASTM E1820 A5.4.

$$K_Q = \frac{P_Q f\left(\frac{a}{W}\right)}{(BB_N W)^{1/2}} \tag{4.9}$$

$$f\left(\frac{a}{W}\right) = \left(\frac{\zeta}{\varsigma}\right)\left[C_0 + C_1\left(\frac{a}{W}\right) + C_2\left(\frac{a}{W}\right)^2 + C_3\left(\frac{a}{W}\right)^3 + C_4\left(\frac{a}{W}\right)^4\right] \tag{4.10}$$

For a compact tension C(T) specimen, the geometric parameters for stress intensity factors are:

ζ	ς	C_0	C_1	C_2	C_3	C_4
$2 + \frac{a}{W}$	$\left(1 - \frac{a}{W}\right)^{3/2}$	0.886	4.64	-13.32	14.72	-5.6

Table 4.2: Parameters for stress intensity factor for C(T) specimen.

where P_Q is the critical load described in Figure 4.6, $f\left(\frac{a}{W}\right)$ is a dimensionless function of the size of the specimens, B is specimen thickness, B_N is net specimen thickness if side groove is present, and W is the width of the specimen. Fracture toughness K_{Ic} equals to K_Q if and only if the following qualification requirements are met according to ASTM 1820-01.

$$K_{Ic} = K_Q \tag{4.11}$$

$$If\ and\ only\ if\quad \frac{P_{max}}{P_Q} \leq 1.10 \tag{4.12}$$

$$and\quad 2.5\left(\frac{K_Q}{\sigma_Y}\right)^2 < b_o \tag{4.13}$$

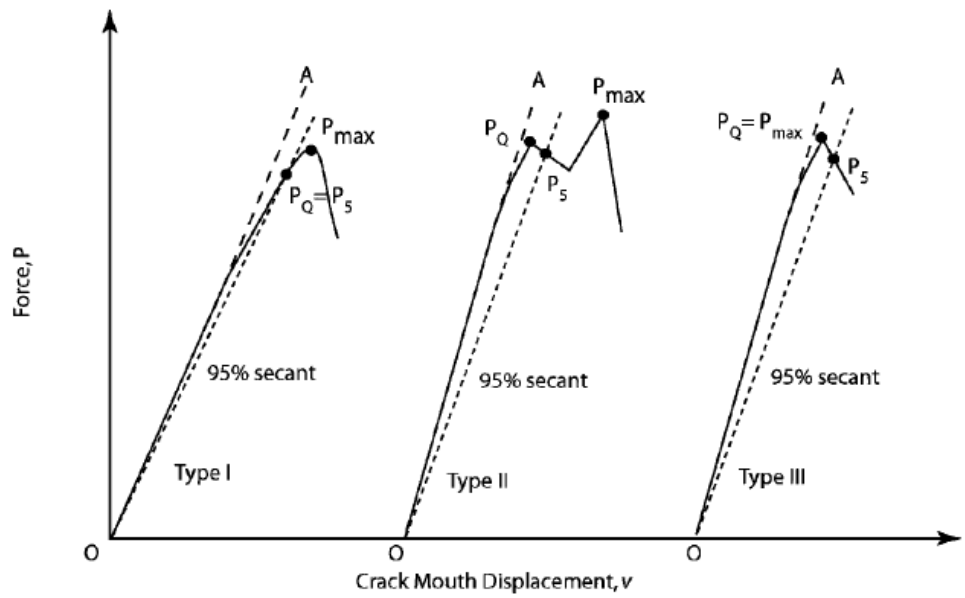

Figure 4.6: Definition of the critical load in fracture toughness test.

Another way to estimate the fracture toughness of the rotor material is by converting J_{Ic} using Equation 4.14. This method assumes the elastic conditions are valid for the material. For nonlinear elastic materials such as steel, it usually overestimate the fracture toughness value.

$$K_{JIc} = \sqrt{E' J_{Ic}} \tag{4.14}$$

The calculated values of the fracture toughness values and J-integral values for both center and surface material specimens are summarized in Table 4.3.

CT specimens	J_{Ic} $[KJ/M^2]$	K_{JIc} $[MPa]$	K_{Ic} $[MPa]$
Center	31	84	77
Surface	42	98	88

Table 4.3: Material fracture toughness tests results.

The fracture toughness values of center material and surface material of the rotor are expected to have slight difference due to its heat treatment and thickness. Identical tests were repeated to obtain an average measurement of crack initiation stress intensity factor and fracture toughness value.

4.3 Fatigue Crack Propagation Test

Most applications of energy storage systems require frequently storing and releasing energy. One of the advantages of flywheel energy storage is long life cycles compared to other types of energy storage. The rotor are usually designed to operate at a speed that the maximum stress in the rotor is less than the tensile strength of the material to avoid fracture. However, the rotor may still fail due to fatigue under cyclic load. Flaws imbedded within the material are potential sites for cracks development depending on the size of the flaws and the stress. Fatigue crack propagation tests characterize the crack propagation within a cyclic stress field.

Four compact tension samples were made out of a test block of rotor material from both the surface and the center of the block. The samples were machined into compact tension specimens with respect to the requirements in ASTM Standard E647.7 which requires that the behavior of the specimen be predominantly elastic during the tests. For a C(T) specimen, the following requirement was met.

$$W - a \geq \frac{4}{\pi}\left(\frac{K_{max}}{\sigma_Y}\right)^2 \tag{4.15}$$

where K represents the stress intensity factor which is defined as:

$$K = f\left(\frac{a}{W}\right)\sigma\sqrt{\pi a} \tag{4.16}$$

$f\left(\frac{a}{W}\right)$ is a dimensionless geometric function of the size of the test specimen. For a C(T) specimen shown in Figure 4.4, this function is defined as:

$$f\left(\frac{a}{W}\right) = \frac{2 + \frac{a}{W}}{\left(1 - \frac{a}{W}\right)^{3/2}}\left[0.886 + 4.64\left(\frac{a}{W}\right) - 13.32\left(\frac{a}{W}\right)^2 + 14.72\left(\frac{a}{W}\right)^3 - 5.60\left(\frac{a}{W}\right)^4\right] \tag{4.17}$$

The tests were performed using a stress ratio of $R_s = 0.1$ and maximum stress intensity factor K_{max} less than 60 $MPa\sqrt{m}$.

$$R_s = \frac{K_{min}}{K_{max}} \tag{4.18}$$

$$\Delta K = K_{max} - K_{min} \tag{4.19}$$

The tests and analysis procedures followed the constant load amplitude tests (K-increasing) procedures in ASTM E647. The tests were performed under room temperature (70^oF), and the relative humidity was about 25%. The loads applied on the specimens were in the haversine waveform at the frequency of 10 Hz. Crack surface of the fatigue crack propagation test specimen is shown in Appendix B. Figure 4.7 illustrates crack length vs. N curves.

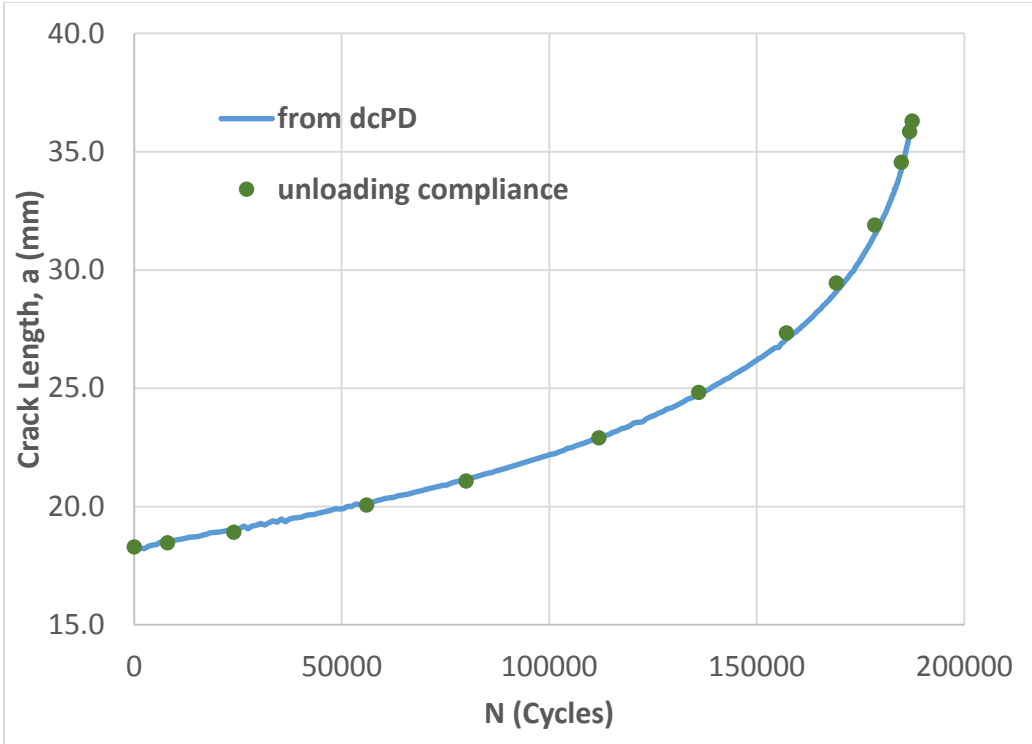

Figure 4.7: Fatigue crack growth curves of C(T) specimen of a rotor material.

The crack growth rate $\frac{da}{dN}$ can be interpreted by numerically differentiating this curve.

$$\frac{da}{dN} = \frac{a_{i+1} - a_i}{N_{i+1} - N_i} \tag{4.20}$$

The calculated fatigue crack growth rate $\frac{da}{dN}$ versus the change in stress intensity factor ΔK are plotted in Figure 4.8. The test captured the stable propagation phase of the fatigue crack. The crack initiation phase and the unstable accelerated crack growth phase were not obtained in this test.

The Paris's Law describes the power law relationship for fatigue crack growth in the stable crack propagation region where the fatigue crack growth rate depends only on ΔK. The equation that fits the experimental data of the rotor material is given by:

$$\frac{da}{dN} = C(\Delta K)^m \quad \left[\frac{mm}{cycle}\right] \tag{4.21}$$

$$C = 1.485 \times 10^{-8} \quad \left[\frac{mm}{cycle \cdot MPa\sqrt{m}}\right] \tag{4.22}$$

$$m = 2.827 \tag{4.23}$$

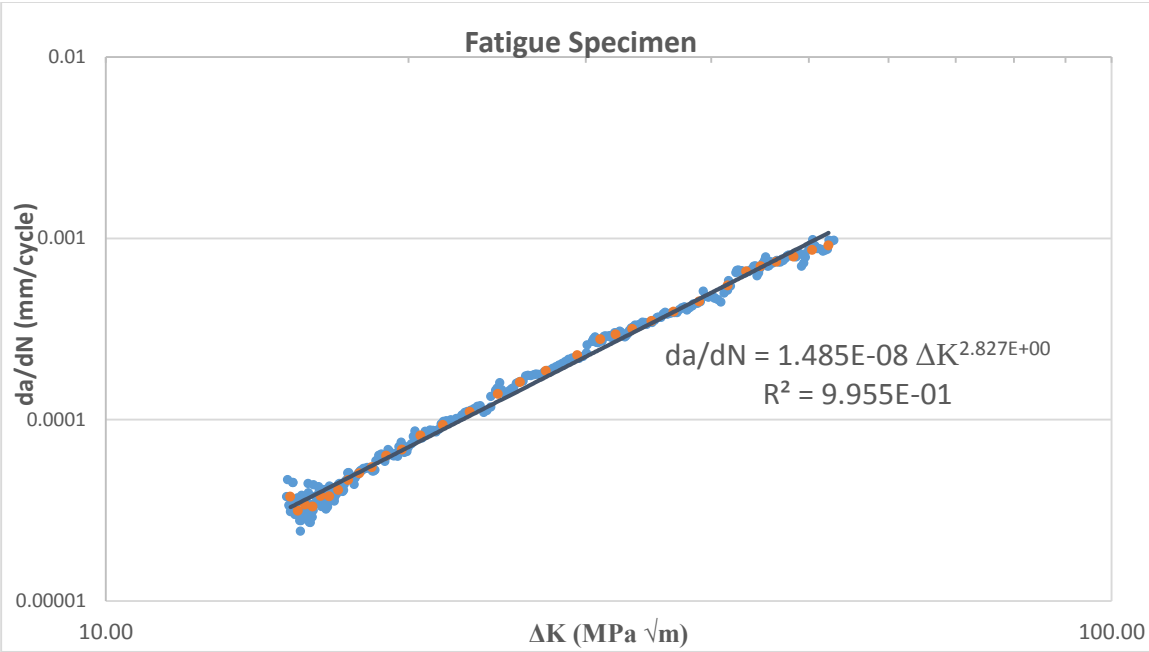

Figure 4.8: Fatigue crack growth behavior in rotor steel.

A more general relationship between the crack growth rates and the stress intensity that characterizes the fatigue crack growth in most materials can be expressed in terms of both K_{max} and ΔK. [23, 24]

$$\frac{da}{dN} = C'(K_{max})^n(\Delta K)^p \tag{4.24}$$

$$where \quad C' = C(1-R)^n \tag{4.25}$$

$$and \quad n + p = m \tag{4.26}$$

In brittle materials, such as ceramics, the component n is much larger than p, and the crack growth rate is K_{max} controlled. In ductile materials, the component p is much larger than n, which makes the crack growth rate to be ΔK controlled. Since the rotor material is ductile steel, we can ignore the contribution of K_{max}, and therefore the Paris' Law is a representative equation to characterize the relationship between crack growth rates and stress intensity.

This equation can be integrated from the initial crack length to critical crack length to predict the life cycles of the rotor, which will be shown in the later chapter.

5. Rotor Stress Analysis

Stress analysis is one of the most important steps for rotor design. Designing the geometry and rotational speed that minimize the stress level of the rotor can increase the safety margin against rotor catastrophic failure and extend the lifetime expectancy of the flywheel system. Theoretical analysis of stress and strain distribution of the rotor was shown in Chapter 2. However, theoretical calculation of stress and strain within a rotor with complex profile is very difficult since the profile function of the rotor geometry is usually a discrete function. Finite element method is applied in this chapter to calculate the stress and strain distribution within complex shaped rotors. The effect of heat treatment on residual stress in the rotor will be analyzed. A baseline rotor geometry for analysis is shown in Figure 5.1. Optimization of the rotor geometry is conducted based on the input of stress analysis using finite element analysis. In addition, the resonant modes and frequencies of the rotor are obtained by calculating eigenvalues and eigenvectors of the rotor geometry in dynamic analysis. Finally, comparison of a thick rotor and a rotor of many thin discs will be looked into. This analysis were done in Abaqus CAE as the finite element code and mesh generator.

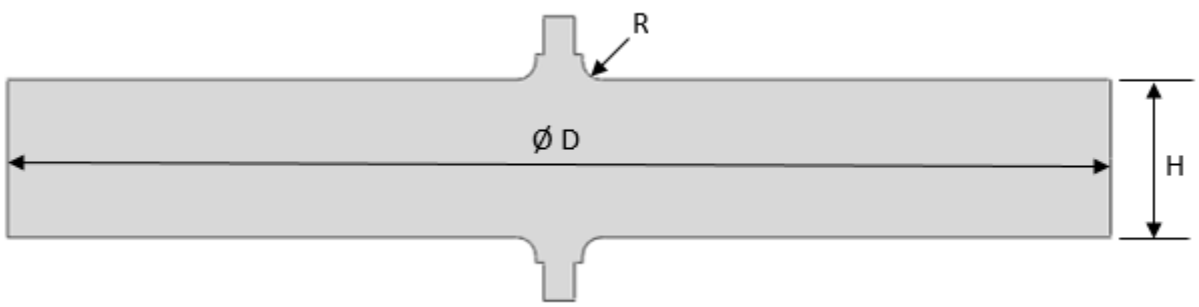

Figure 5.1: Baseline rotor geometry for flywheel energy storage.

5.1 Effect of Heat Treatment and Residue Stress

The rotor material is chosen to be AISI 4340 steel. Many methods of heat treatment can be created for 4340 steel. A typical heat treatment process involves austenitization for one hour in inert Argon atmosphere at temperature in the range of 870 to $1200^{o}C$ followed by cooling to $870^{o}C$ and holding for one hour before quenching. Next the material is quenched into room temperature oil, or ice-water, or an agitated ice-10 percent brine solution. Then tempering was carried out in Argon atmosphere at a temperature ranging from 200 to $450^{o}C$ for usually 2 hours. [25-27]

Due to the thickness and geometry of the rotor, the temperature distribution throughout the rotor may not be kept homogeneous which leads to formation of non-uniform microstructure and induces residual stress. A 2D transient coupled temperature-displacement finite element model which models the heat transfer and stress of the rotor during the heat treatment process was built in ABAQUS CAE to study the temperature and stress distribution versus time. The rotor was meshed with 1730 CPE4T elements which are 4-node plane strain thermally coupled quadrilateral elements that model bilinear displacement and temperature. Figure 5.2 shows the temperature distribution within the rotor instant after quenching the rotor from $870^{o}C$ to $200^{o}C$. The heat

transfer coefficient of 4340 steel is a function of temperature. [28] In this finite element analysis, the surface heat transfer coefficient is assumed to be a constant 7 $kWm^{-2}K^{-1}$ which is taken as the average in the temperature range between 200^oC to 800^oC.

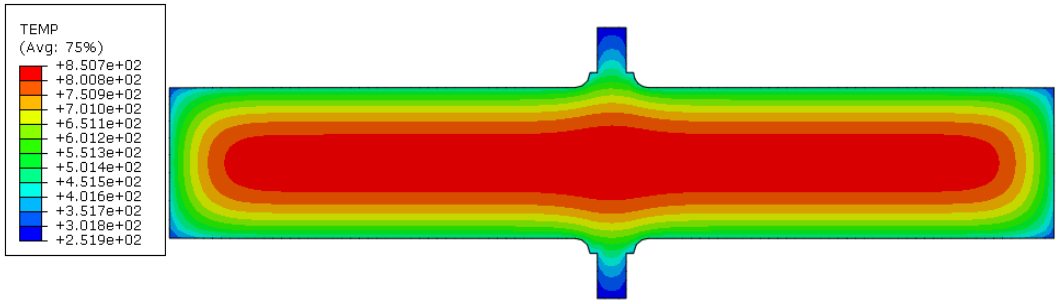

Figure 5.2: Temperature distribution in the rotor instant after quenching.

As shown in the figure above, the temperature gradient is fairly large which leads to large stress and strain in the rotor. The stress is large enough that residual stress are created on the surface layer of the rotor. Residual stress can be modeled in the finite element model assuming the rotor material has homogeneous properties. Figure 5.3 shows the distribution of equivalent plastic strain in the rotor after quenching from 870°C to 200°C.

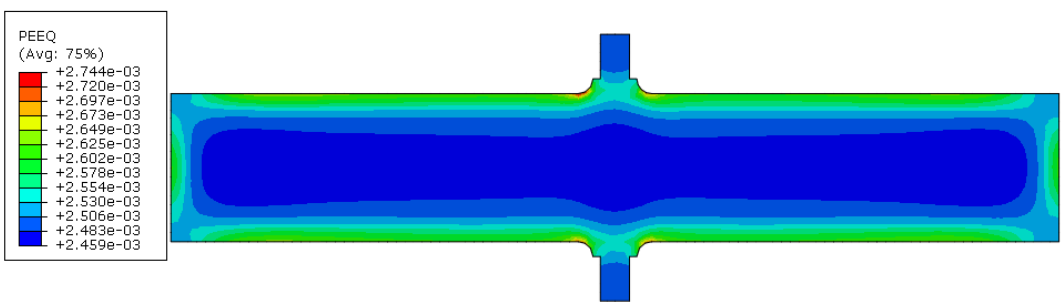

Figure 5.3: Distribution of equivalent plastic strain within the rotor after quenching from 870 degree C to 200 degree C.

After the rotor returns to room temperature, residual stress exists where the material has plastically deformed. The surface of the rotor yielded in tension during the quenching and will have compressional residual stress. However, the model does not model the microstructure variance due to the different cooling rate throughout the rotor. A more accurate FEA model which models the phase changes in microstructure of the material will give a better understanding of the residual stress.

5.2 Steel Rotor Finite Element Analysis

First, consider a rotor with diameter of 70 inches and thickness of 10 inches. The rotor has top and bottom shafts for fitting with the bearings and vacuum seals. Radius were designed where the shafts meet the surfaces of the rotor as shown in Figure 5.1 for the purpose of reducing local stress concentration. The rotor is made of 4340 steel whose mechanical properties are summarized in

Table 5.1. The mechanical properties were obtained from the material tensile test shown in Chapter 4. The rotor material is assumed to be homogeneous with the properties of the center material samples. These properties will be the inputs for finite element analysis to characterize the rotor material.

Mechanical Properties	Elastic Modulus (GPa)	Yield Strength (MPa)	Ultimate Tensile Strength (MPa)	Elongation	Thermal conductivity (W/mK)
4340 Rotor Steel	205	1200	1350	0.11	44.5

Table 5.1: Mechanical properties of rotor material - 4340 steel.

The linear interpolated stress vs. strain curve is shown in Figure 5.4 which is the characterizing model of the rotor material inputted in the finite element analysis.

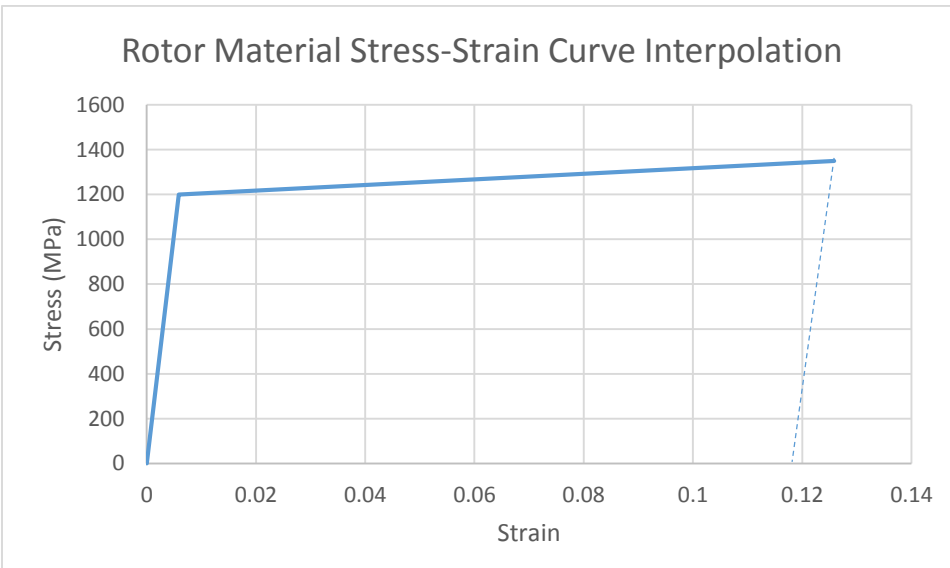

Figure 5.4: Linear interpolation of stress-strain curve of rotor material in finite element analysis.

Since the rotor geometry and the loadings on the rotor are axisymmetric, the analysis can be simplified to 2D with properly defined boundary conditions. Therefore, the rotor is represented by half of a cross section of the rotor. 2D analysis has the advantage of less number of elements and easier for calculation. Therefore, the mesh size of the 2D model can be much smaller than 3D which improves the accuracy of the analysis. The finite element model has 31831 linear quadrilateral elements of type CPS4R. CPS4R is a 4-node bilinear plane stress quadrilateral element type for reduced integration and hourglass control.

The rotor is under centrifugal force due to rotation and therefore rotational body force corresponding to specific rotational speed is applied as the loading condition. The following boundary conditions are built into the model: (i) radial displacement on the rotation axis at $r = 0$ is zero; (ii) displacement and rotation at the center point is zero; (iii) stress at the outer radius is

zero. The boundary conditions and loading conditions are shown in Figure 5.5. The first two boundary conditions can be specified by restricting the displacement in the radial direction of the rotation axis to be zero and encastre at the center point shown as red in the figure.

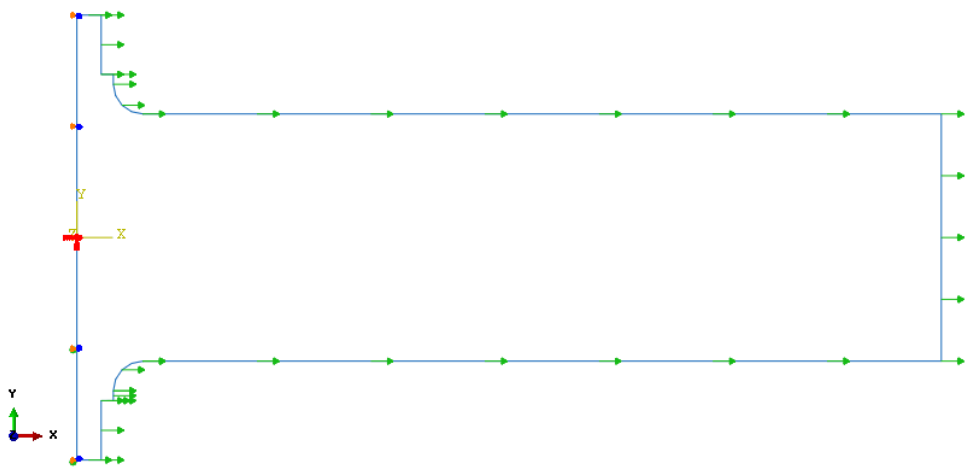

Figure 5.5: Boundary conditions and loading conditions of 2D rotor finite element analysis.

The rotational speed of the rotor was modeled as a linear ramp function from 0 RPM to maximum speed when the maximum stress reached the ultimate tensile strength of the material. Figure 5.6 (a) indicates the stress distribution of the rotor when local material yielding first initiated at the radius of the shafts. Three stress concentrated areas were found at the radius and at the center of the rotor as shown in Figure 5.6 (b). The stress shown is the Von Mises stress calculated with both radial stress and hoop stress as in Equation 5.1. Figure 5.6 (c) shows the equivalent plastic strain (PEEQ) distribution before the rotor fractures. Equivalent plastic strain is calculated by:

$$\varepsilon_e^p = \frac{2}{3}\sqrt{\frac{1}{2}\left[\left(\varepsilon_{11}^p - \varepsilon_{22}^p\right)^2 + \left(\varepsilon_{22}^p - \varepsilon_{33}^p\right)^2 + \left(\varepsilon_{33}^p - \varepsilon_{11}^p\right)^2\right] + \left[\left(\varepsilon_{12}^p\right)^2 + \left(\varepsilon_{23}^p\right)^2 + \left(\varepsilon_{31}^p\right)^2\right]} \quad (5.1)$$

The stress level at the radius areas is higher than at the center. Compared to a constant thickness disc rotor, the higher stress and larger sample volume increase the possibility of rotor failure. Therefore, rotor shape optimization should be considered with the goal of eliminating the stress concentration at the radius areas and lowering the stress level at the center.

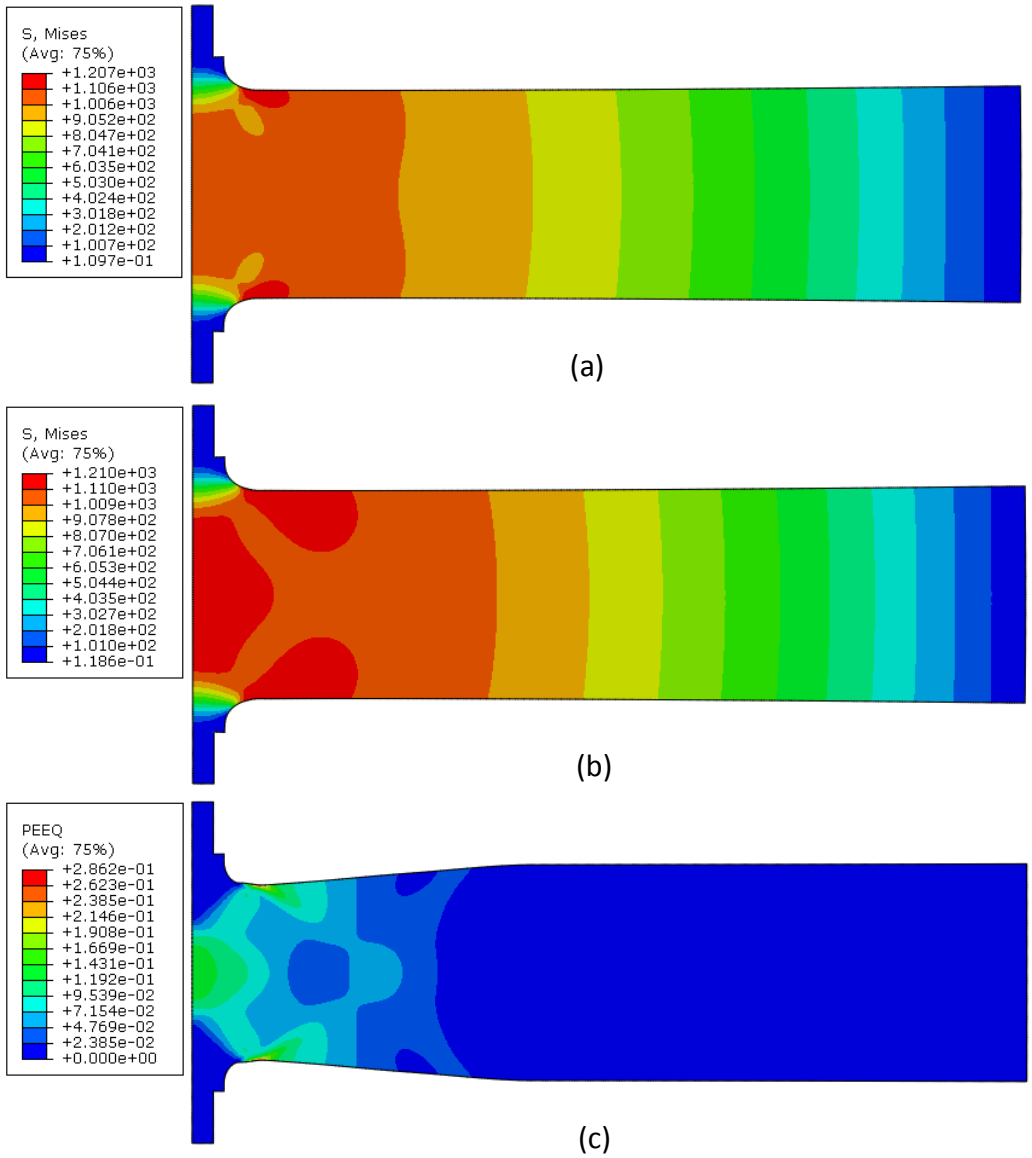

Figure 5.6: Stress distribution of 2D rotor FEA model at (a) yield initiation locations; (b) stress concentration zones; (c) plastic Strain distribution before fracture.

5.3 Optimization of Rotor Geometry

Shape optimization of flywheel has been studied. As shown before, the energy density of the rotor is dependent on the rotor design and rotor material properties. Shape factor K is a constant defined to characterize the geometrical configuration of the rotor. It relates the energy density of the flywheel energy storage system to the material properties:

$$e = \alpha' \alpha'' \alpha''' K \frac{\sigma_u}{\rho} \tag{5.2}$$

α' is the safety factor against burst. α'' is the depth of charge and discharge which is the ratio between the usable portion of the energy and the total energy capacity. And α''' is the ratio between the weight of the rotor and the weight of the entire flywheel energy storage.

In addition, speed factor ξ is defined as the ratio between the angular speed of the rotor and the angular speed of a thin rim that has the same outer diameter and density under the same stress. Several shapes of rotors as well as the corresponding shape factors and speed factors are shown in Figure 5.7.

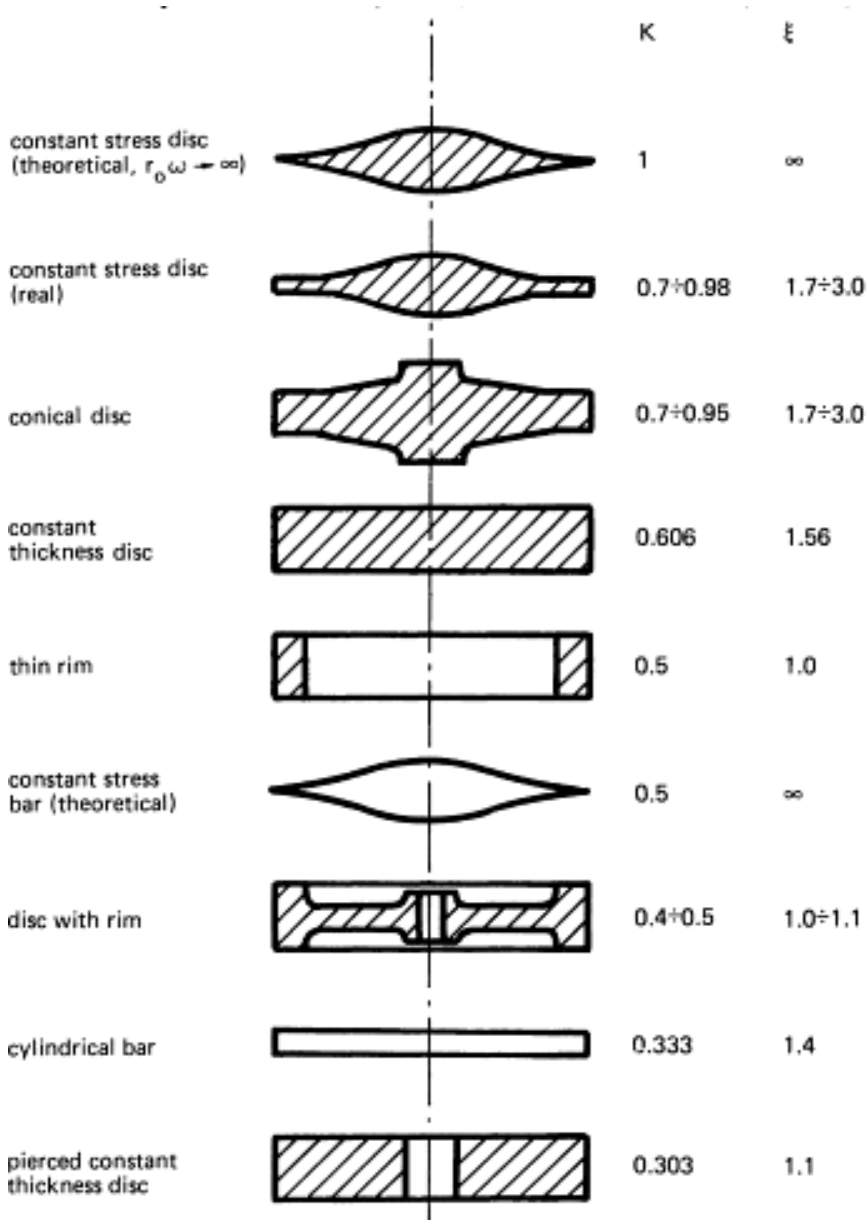

Figure 5.7: Possible rotor shapes and corresponding shape factors K and speed factors $\boldsymbol{\xi}$. [29]

To reduce the surface stress concentration at the radius areas and also lower the stress level at the center, the rotor shape is modified to have a large radius which is close to a conical disc. The finite

element model for this modified rotor shape used the same type of elements and kept the boundary and load conditions the same. Figure 5.8 shows the stress distribution within the rotor at the speed when the rotor first yield at the center.

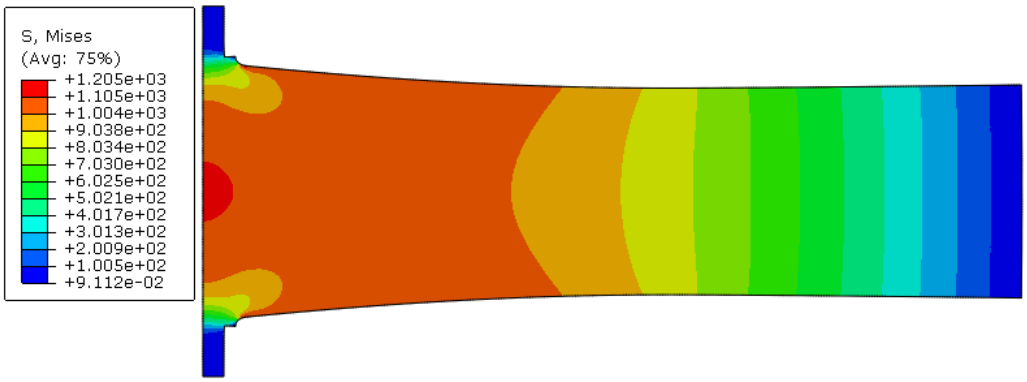

Figure 5.8: Finite element analysis of stress distribution within the optimized rotor shape when the center of the rotor first yields.

Compared to the simple disc shape rotor, this new rotor geometry does not have the surface stress concentration, the stress level is lowered at the center, and the zone of yielding is smaller under the same rotational speed. To confirm the result of the 2D finite element analysis, a 3D FEA model of the rotor was built to compare the result of stress distribution at same speed. As shown in Figure 5.9, both 2D and 3D FEA models show similar results of stress distribution.

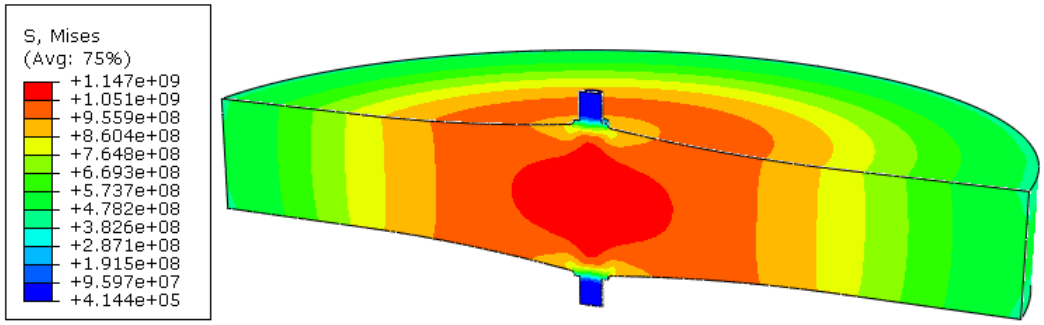

Figure 5.9: 3D finite element analysis of the rotor shows the stress distribution that are similar to 2D results.

5.4 Rotor Dynamic Analysis

Due to the dynamic nature of a fast rotating rotor, the resonance of the rotor can affect the structural stability of the whole flywheel energy storage system. The rotor design has to meet the requirement that the resonant frequency of the rotor is above the range of operating frequencies. A 3D finite element model of the rotor was built to calculate the dynamic response of the rotor. The model consisted of 77052 C3D10 elements (A 10-node quadratic tetrahedron element). Resonant frequencies under 200 Hz were calculated. The first resonant model is shown in figure which happens at the frequency of 103 Hz.

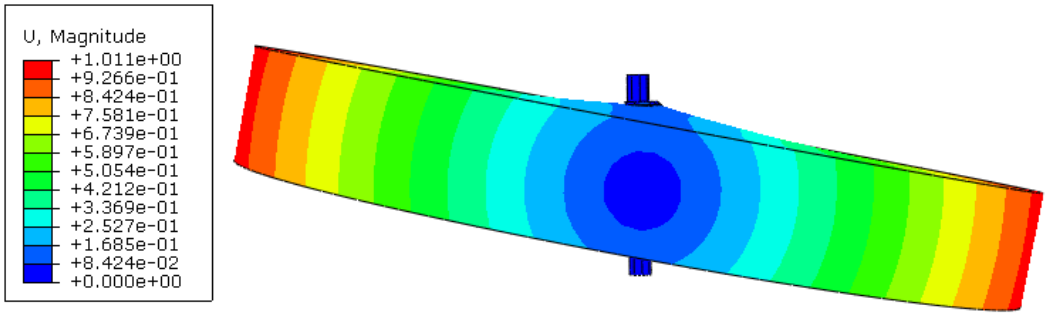

Figure 5.10: 3D Finite element analysis shows the first resonant model of the rotor @ 103 Hz.

5.5 Experimental Validation of Finite Element Analysis

Finite element analysis has shown the stress distribution in a rotor at certain speed, which determines the design of the shape and speed of the rotor. To evaluate the results of the finite element analysis, rotor need to be tested experimentally. Testing on large scale rotors to their maximum speeds is dangerous and costly. However, it is shown in the previously that the maximum stress in the rotor is a linear function of the tip speed of the rotor. And therefore, a small-scale rotor which rotates with the same tip speed and geometry can have the same stress level. The following Figure 5.11 shows the FEA results of the rotational speeds of small-scale rotors at which their maximum stress reaches tensile strength of the 4340 steel.

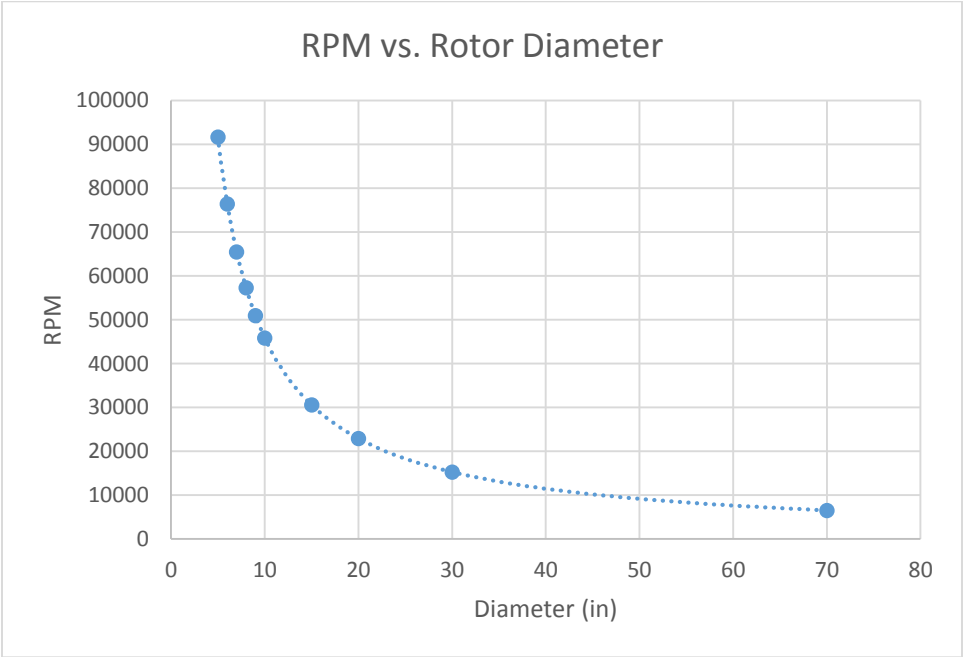

Figure 5.11: Rotational speeds for the maximum stress of small-scale rotors to reach tensile strength of 4340 steel.

A testing system was built for testing a 5.5 inch diameter rotor. The small rotor was made out of 4340 steel and machined to the same shape as the actual rotor. The rotor was connected to an air

motor with maximum speed of 100,000 rpm. The rotor was kept inside vacuum (~0.1mbar) to reduce the drag. Optical encoder was installed next to the shaft of the rotor to read the rotational speed of the rotor. The whole test system was operated inside a concrete containment to prevent possible damage due to rotor failure. The model of the test system and the actual built-up are shown in Figure 5.12.

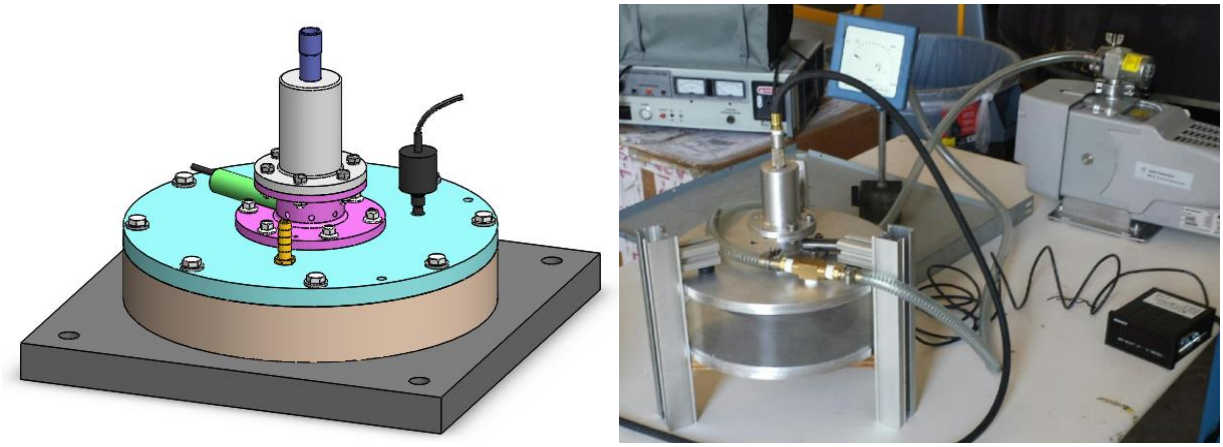

Figure 5.12: Small scale rotor testing system model and experimental setup.

Rotational speed and vacuum pressure were feedback controlled. The control scheme of the system is shown in Figure 5.13.

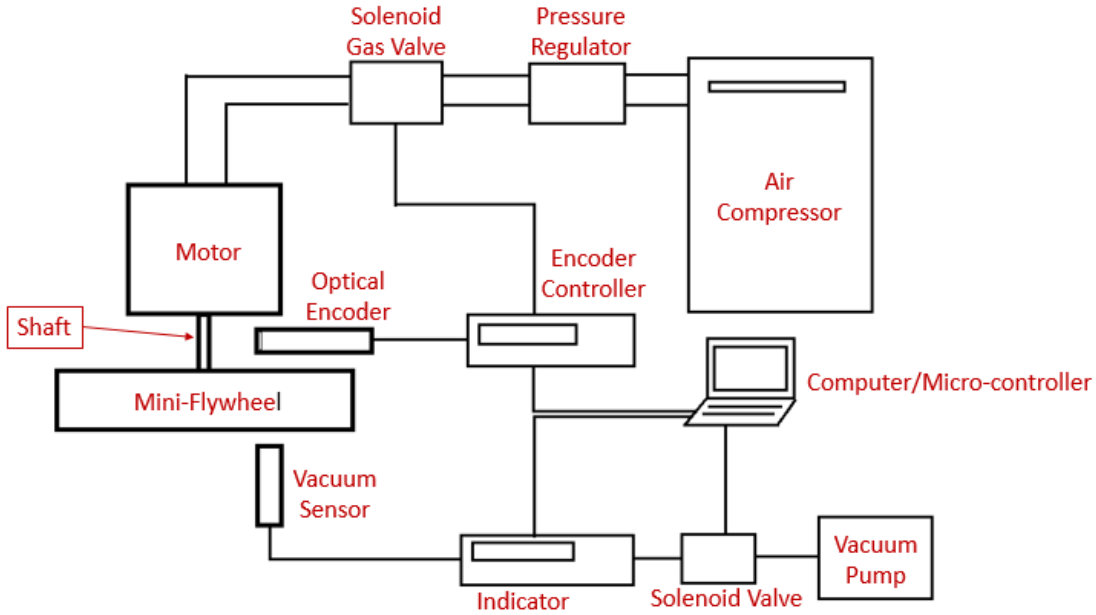

Figure 5.13: Control schematic diagram for the small scale rotor testing system.

This test system can have the following three functions: 1) evaluating the finite element analysis by spinning the rotor to fracture and comparing the result with FEA model prediction; 2) generating S-N curve of the rotor by obtaining the lifecycles of rotors spinning up to different

maximum speeds; 3) evaluating the theoretical calculation of power loss due to aerodynamic drag on the rotor which will be shown in Chapter 7.

6. Failure Analysis

A rotor with large mass rotating at a high speed has large kinetic energy. Consequences of a catastrophic rotor failure can be dramatic since the broken pieces from the rotor have huge inertia and momentum that can break the containment and cause further damages. An understanding of the mechanisms of rotor failure is critical for designing flywheel energy storage system. Rotors can have catastrophic failure due to many causes, such as over-speeding, fatigue crack propagation, and subsystem failures. Typical rotor failure modes have been characterized though experimental works. Analysis of fracture mechanics is discussed in this chapter to relate the material properties and conditions to rotor failure events. Material properties obtained from material characterization tests in the previous chapter will be implemented into the analysis. Fracture criteria will be derived from the analysis to aid designers developing safer rotors. Finally, the consequences of broken pieces of fractured rotor penetration surrounding containments will be discussed to help the design of a safe containment for the flywheel energy storage.

6.1 Failure Modes

As shown by the analytical and finite element analysis in the previous chapter, a spinning steel rotor has high stress level in the center area as well as at the stress concentrated area around the shaft radius. Stress is the main reason for rotor failure in many aerospace and flywheel energy storage applications. There are two types of failure caused by stress: fracture and fatigue. High rotational speed can cause the stress level at certain location of the rotor to be higher than the tensile strength of the rotor material which leads to sudden rupture of the rotor. In addition, cyclic loadings due to the work load of the flywheel energy storage system can develop a fatigue crack in the rotor and eventually catastrophic failure.

For both types of failure, the fracture or crack initiates at the most stresses areas. Machined features and interfaces such as drilled hole, groove and radius tend to develop stress concentration which are more prone to fracture. Steel rotors tend to break into large pieces. Studies were conducted to predict how rotors break and evaluate the number of fragments generated by the burst. [30-33] Fractures can be categorized into two main types: hoop mode and rim peel mode shown in Figure 6.1.

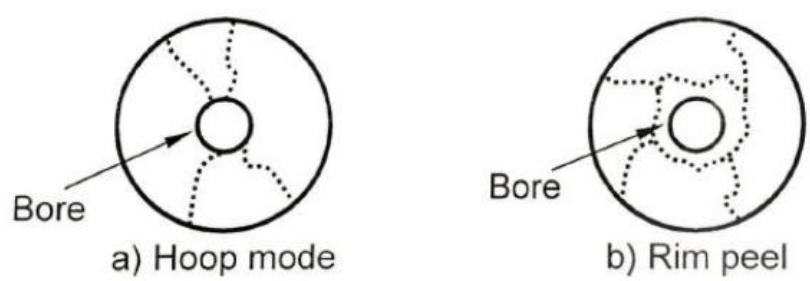

Figure 6.1: Failure modes of a spinning rotor a) hoop mode, b) rim peel. [34]

The study of rotor failure modes were conducted with rotors with a center bore which induced stress concentration. For our interest, rotors in flywheel energy storage have top and bottom shafts which can also generate stress concentrated area around the shafts, and therefore the failure modes shown in Figure should be representative.

6.2 Fracture Mechanics of Rotor

Steel rotors fracture due to an unstable crack developed under high stresses caused by high rotational speed. The crack initiates from defects such as micro-cracks, voids and grain boundaries which can induce local stress concentration around them.

In steel, crack growth is mainly promoted ahead of the crack tip by intrinsic microstructural damage mechanisms. One model to characterize the stress and strain distribution ahead of the crack tip is given by the HRR singularity. [35] J-integral is established as a stress amplitude parameter within the plastic zone. The crack starts to propagate to cause fracture when J-integral exceed the critical value J_C. In chapter 4, we have found the fracture toughness J_{Ic} for the rotor material and the corresponding stress intensity factor K_{JIc} and K_{Ic}. Stress intensity factor K is defined as:

$$K = F\sigma\sqrt{\pi a} \tag{6.1}$$

Where F is a geometric function of the size and configuration of the crack in the component. [36]

$$F = \begin{cases} 1.12 & for\ embeded\ crack \\ 1.27 & for\ surface\ crack \end{cases} \tag{6.2}$$

As shown in the equation of stress intensity factor, the driven force for crack to propagate depends on both the stress level around the crack as wells as the crack size. To determine the burst speed at which the defects inside the rotor will cause the rotor fracture, the size of the defects has to be measured. The methods of detecting defects and flaws inside a large rotor using nondestructive ultrasonic inspection will be discussed later in this chapter.

Once the initial size of the defects a_i in the rotor are quantified, the stress that can cause the sudden fracture of the rotor σ_f is given by:

$$\sigma_f = \frac{K_{Ic}}{F\sqrt{\pi a_i}} \tag{6.3}$$

In many cases of flywheel energy storage designs, the maximum rotational speed of the rotor is limited by the subsystems and design requirements. Assume the maximum rotational speed is fixed, and therefore, the maximum stress σ_{max} that the rotor will undertake is fixed. The critical crack length over which the crack becomes unstable and causes rotor fracture is given by:

$$a_c = \frac{1}{\pi}\left(\frac{K_{Ic}}{F\sigma_{max}}\right)^2 \tag{6.4}$$

The initial detectable defect size a_i and a_c will be implemented later into the estimation of the lifetime of the rotor. For rotor design, both yield criteria and fracture mechanics should be considered to determine the geometry and rotational speed of the rotor.

6.3 Rotor Inspection and Health Monitoring

Flaws inside the rotor can cause rotor failure under static and cyclic loading conditions. Rotor inspection and health monitoring ensure the rotors to be free of flaws that could cause failure. Inspecting flywheel rotor is a challenge to the current inspection technologies because of the large thickness of the steel rotor. There are both destructive and nondestructive inspection methods that are able to inspect a steel rotor for defects. For rotor quality control purposes, the inspection method has to be nondestructive so that the inspection will not induce any damage to the rotor nor to cause potential failure of the rotor during operation. Several nondestructive flaw inspection technologies exist nowadays including the use of x-ray, ultrasound, eddy current, die penetration and etc. Among these methods, ultrasonic flaw inspection enables through-thickness inspection, and by altering the frequency of the ultrasound signal, one can detect flaws of desirable size.

Ultrasonic flaw detection technology is based on the physics that ultrasonic waves traveling in a solid are reflected from flaws and generate clear eco patterns, which is completely nondestructive to the material. The accuracy of ultrasonic flaw detection is characterized by the minimum detectable flaw size. Minimum detectable flaw size d_0 is defined as half the wavelength of the ultrasonic wave which depends on the material of the test object, the type of ultrasonic wave, and the frequency of the transducer as shown in the equation below:

$$d_0 = Minimum\ detectable\ flaw\ size = \frac{\lambda}{2} = \frac{c}{2f} \tag{6.5}$$

where c is the speed of ultrasonic wave in the test material , and f is the frequency of the transducer.

For our application, the rotor is made of 4340 steel. The speed of longitudinal wave in 4340 steel, c_L, is $2.305 \times 10^5\ in/sec$. The speed of shear wave in 4340 steel, c_S, is $1.272 \times 10^6\ in/sec$. Longitudinal wave travels twice the speed of shear wave. Longitudinal wave provides the depth of inspection, and can be used to detect defects in a large sized component. While shear wave offers smaller minimum detectable size, it offers accurate detection of small defects. The frequency of the transducers used for the inspection, f, is 10 MHz. Therefore, the minimum detectable flaw sizes are calculated as:

$$d_l = \frac{\lambda_L}{2} = \frac{2.305 \times 10^5\ in/sec}{2(10\ MHz)} = 0.012\ in = 0.3\ mm \qquad for\ longitudinal\ wave \tag{6.6}$$

$$d_s = \frac{\lambda_S}{2} = \frac{1.272 \times 10^5\ in/sec}{2(10\ MHz)} = 0.006\ in = 0.15\ mm \qquad for\ shear\ wave \tag{6.7}$$

Flaws of different orientations were inspected by changing the angle of the ultrasonic signal. The inspection covered the high stress region of the rotor as shown in Figure 6.2.

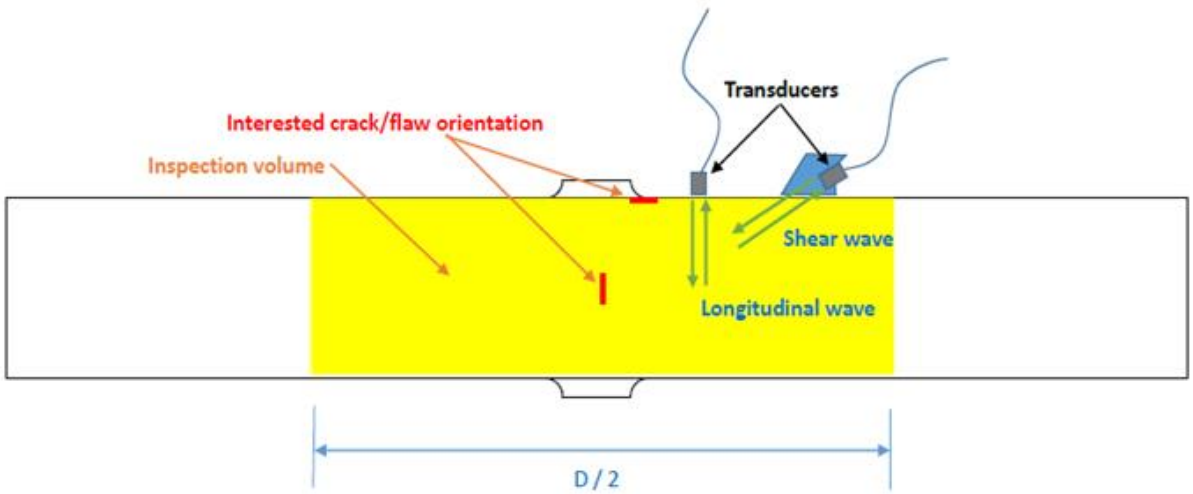

Figure 6.2: Ultrasonic flaw inspection plan for rotor in flywheel energy storage.

Calibrating for the ultrasound transducer and receiver was done on a reference block that were made of the same material as the rotor. The block was made to 10 inch by 10 inch by 1 inch to represent the thickness of the rotor. Nine 0.3 mm holes were machined along the 10 inch length of the block to simulate defects at different depth of the rotor. The rotor was firstly scanned with the straight beam transducer in a tight grid pattern covering more than the interested inspection volume shown as the yellow area in Figure 6.2 above. Then, a 60 degree angled beam transducer and a 70 degree angled beam transducer both coupled with Lucite sound media blocks were used to detect vertical and angled flaws within the interested inspection volume. No feedback signals ever showed on the detector that were comparable to the feedback signals of the reference blocks. Later, to confirm the results, the rest of the volume were also inspected with straight beam and angled beam, and no indications of flaws were found. Therefore, the rotor does not have any flaws of sizes comparable to either the minimum detectable flaw size 0.3mm or the size of the side holes on the reference blocks. The inspection methods and procedures followed the requirements in AMS Standard 2154.

$$d_0 = d_l = 0.3mm \tag{6.8}$$

The minimal detectable flaw size d_0 will be the assumption of the initial crack size $2a_i$ within the rotor.

$$a_i = \frac{d_0}{2} \tag{6.9}$$

6.4 Fatigue Life Analysis

Flywheel energy storage requires the rotor to cycle between high rotational speed and low rotational speed. The cyclic load due to rotation can cause cracks to initiate from defects within the rotor and propagate until a crack grows to the critical length and causes catastrophic failure of the rotor. To estimate the lifetime of the rotor, we have to look into the fatigue behavior of the rotor materials. For steels, there are two damage mechanisms for fatigue crack propagation: intrinsic damage mechanisms ahead of the crack tip, and extrinsic damage mechanisms in the wake

of the crack. The intrinsic damage mechanisms typically involve processes of developing a plastic zone ahead of the crack tip as shown in Figure 6.3 where micro-cracks and micro-voids can be created. In addition, blunting during loading and resharpening during unloading of the crack tip can occur due to the nonlinear behavior of the material. [37, 38] Extrinsic shielding mechanisms result from the creation of inelastic zones surrounding the crack wake or from physical contact between the crack surfaces via wedging, bridging, sliding or the combinations of above. [39]

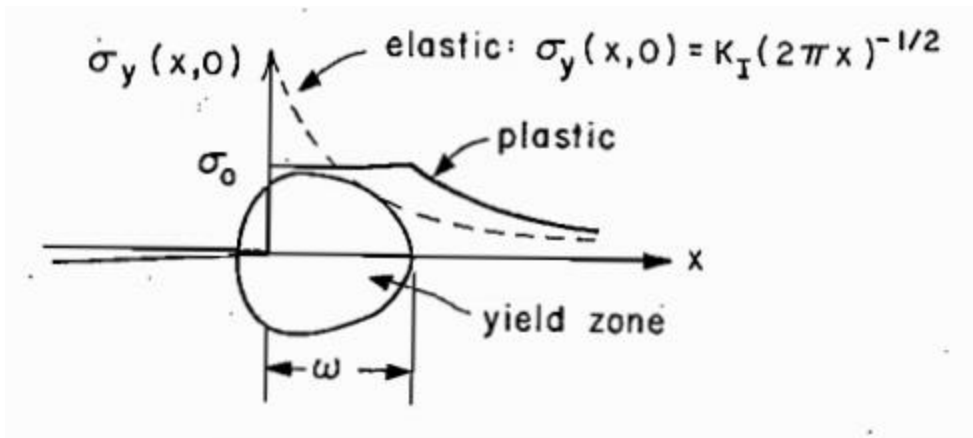

Figure 6.3: Plastic zone developed ahead of crack tip for a hardening material. [39]

The size of the cyclic plastic (yield) zone ahead of the fatigue crack ω is characterized by:

$$\omega = \frac{1}{2\pi}\left(\frac{K_{max}}{\sigma_Y}\right)^2 \tag{6.10}$$

Lifetime of the rotor is estimated based on number of cycles of operation to propagate the miminal detectable crack (defects) a_i to failure at the critical crack size a_c. The Paris' power law Equations 4.21 – 4.23 is obtained from a fatigue crack propagation test on a compact tension specimen of the rotor material provides the relationship between the growth rates of the fatigue crack with the driving stress intensity. By integrating both sides of Equation 4.21 respectively from 0 cycle to the lifetime cycle and from a_0 to a_c for the crack length, the lifetime of the rotor can be calculated as:

$$\int dN = \int_{a_i}^{a_c} \frac{da}{C(\Delta K)^m} \tag{6.11}$$

$$Nf = \frac{2\left(a_c^{\frac{2-m}{2}} - a_i^{\frac{2-m}{2}}\right)}{(2-m)C\left(F\Delta\sigma\sqrt{\pi}\right)^m} \tag{6.12}$$

To more accurately estimate lifetime of the rotor, the crack growth rates vs. stress intensity test data was divided into 4 segments as shown in Figure 6.4, and for each segment, the data was fitted with the Paris' power law equation.

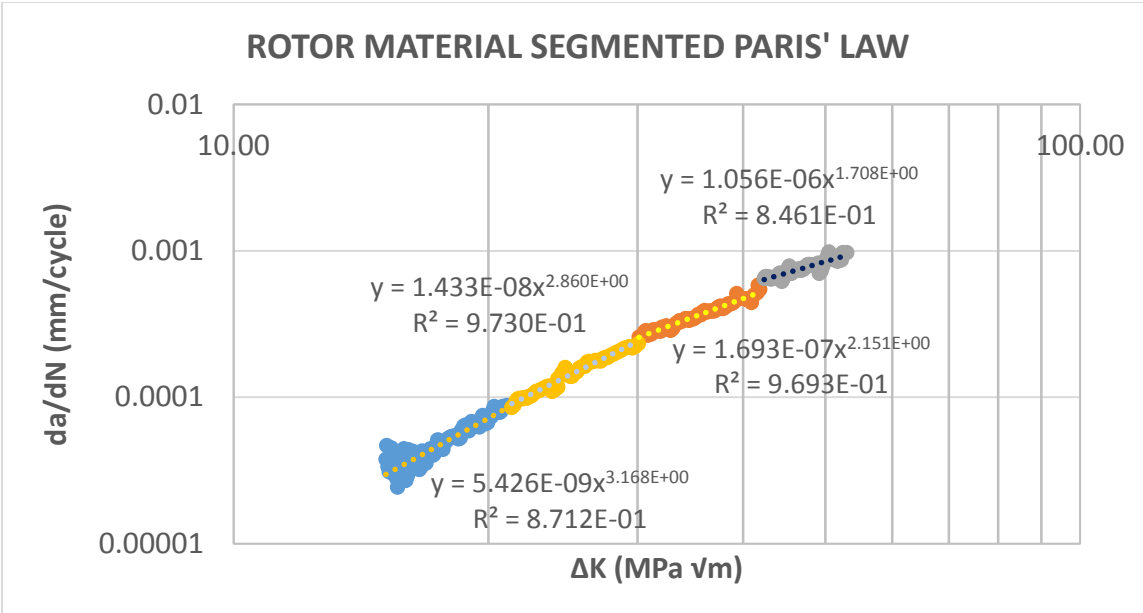

Figure 6.4: Segmentation of the crack growth rate vs. stress intensity data and corresponding Paris' law equations.

Segmentation of $\frac{da}{dN}$ vs. ΔK data	Paris' Law Equation
$\Delta K < 21.25\ MPa\sqrt{m}$	$\frac{da}{dN} = (5.426 \times 10^{-9})(\Delta K)^{3.168}$
$21.25\ MPa\sqrt{m} \leq \Delta K < 30.1\ MPa\sqrt{m}$	$\frac{da}{dN} = (1.433 \times 10^{-8})(\Delta K)^{2.860}$
$30.1\ MPa\sqrt{m} \leq \Delta K < 42\ MPa\sqrt{m}$	$\frac{da}{dN} = (1.693 \times 10^{-7})(\Delta K)^{2.151}$
$\Delta K \geq 42\ MPa\sqrt{m}$	$\frac{da}{dN} = (1.056 \times 10^{-6})(\Delta K)^{1.708}$

Table 6.1: Paris' law equations for the segmented fatigue crack propagation test data: $\frac{da}{dN}$ is in the unit of $\left[\frac{\text{mm}}{\text{cycle}}\right]$.

Flywheel energy storage system is designed to operate within the range from the lowest rotational speed ω_{min} to the highest rotational speed ω_{max}. Since the maximum stress level is proportional to the square of the rotational speed as shown in chapter 2, the range of stress $\Delta\sigma$ is fixed corresponding to the range of rotational speed. And therefore, the variation in stress intensity factor ΔK is given by:

$$\Delta K = F\Delta\sigma\sqrt{\pi a} \tag{6.13}$$

$$where \quad \Delta\sigma = \sigma_{max} - \sigma_{min} = (1 - R_s)\sigma_{max} \tag{6.14}$$

$$\Delta K = (1 - R_s)K_{max} \tag{6.15}$$

The driving force of the fatigue crack propagation ΔK is a function of the stress ratio R_s and maximum stress intensity factor K_{max}. In other words, the design of the maximum rotational speed and lowest rotational speed affects the lifetime estimation of the rotor.

For a simple disc rotor with radius of 35 inches and thickness of 10 inches made out of 4340 steel whose material properties are listed in chapter 5, the lifetime can be estimated by setting the stress ratio and maximum rotational speed. The maximum radial and hoop stresses at the maximum rotational speed appear in the center of the rotor and are calculated as:

$$\sigma_{r_{max}} = \sigma_{\theta_{max}} = \frac{3+\nu}{8}\rho(\omega_{max}R)^2 \tag{6.16}$$

Assume the stress induced by the torque applied by the motor is much smaller in amplitude than the radial and hoop stresses at the center. The effective stress is given by:

$$\sigma_e = \sqrt{\frac{(\sigma_r - \sigma_\theta)^2 + \sigma_\theta{}^2 + \sigma_r{}^2 + 6\tau^2}{2}} = \frac{3+\nu}{8}\rho(\omega_{max}R)^2 \quad at\ r = 0 \tag{6.17}$$

The range of the cyclic stress is then:

$$\Delta\sigma = (1 - R_s)\sigma_e \tag{6.18}$$

The critical crack length of the rotor material is also a function of the maximum rotational speed:

$$a_c = \frac{1}{\pi}\left(\frac{K_{Ic}}{F\sigma_e}\right) = \frac{1}{\pi}\left[\frac{K_{Ic}}{F\left(\frac{3+\nu}{8}\rho(\omega_{max}R)^2\right)}\right] \tag{6.19}$$

Therefore, by plugging Equation 6.19 into the integration of Equation 6.12, the lifetime of this disc rotor can be calculated as shown in Figure 6.5. As the stress ratio R_s increases, the lifetime of the rotor improves. On the other hand, as the maximum rotational speed increases, the lifetime estimation decreases. For rotor of any geometry, as long as the relationship between the stress and rotational speed is determined, the lifetime of the rotor can be estimated following the same procedures.

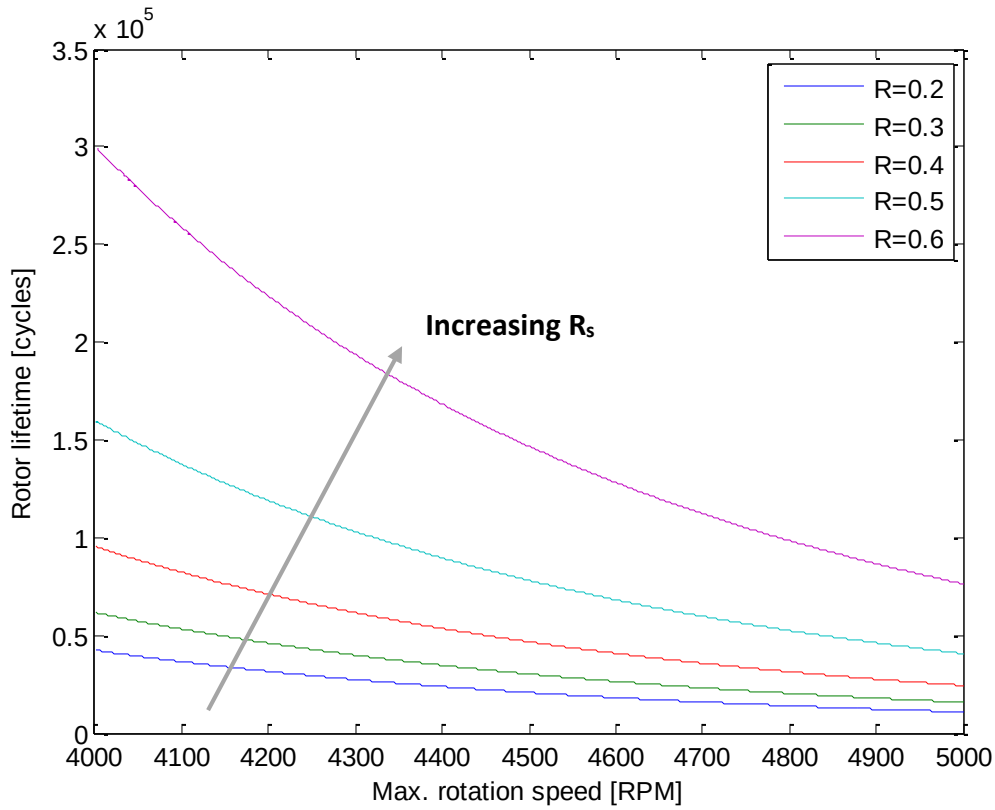

Figure 6.5: Rotor lifetime as a function of stress ratio R_s and maximum roration speed.

6.5 Post Failure Analysis

With the analysis of fracture mechanics, sudden fracture of the rotor due to stress concentration and fatigue can be prevented. However, accidental failures of the rotor can still happen due to other reasons such as subsystem (bearings, seals) failure, deterioration of the material, control fault, and natural disasters. The potential damages caused by rotor catastrophic failure have to be evaluated in order to design safe containment for the flywheel energy storage.

When the rotor breaks, the broken fragments adopt translator and rotational motions. The proportion of the rotor's kinetic energy that is transferred to the fragments as translational energy and as rotational energy depends on the size of the fragments. The larger the fragments are, the more kinetic energy they possess.

Steel rotors tends to break into large pieces when they fail. The fragments have large kinetic energy. Designing the containment structure that avoid any fragment penetration is challenging and also costly for large steel rotors. Therefore, flywheel energy storage systems with steel rotors are commonly installed in special designed vaults under the ground level. When rotors fail, the fragments penetrate through the vacuum chamber and impact into the surrounding soil. It is necessary to estimate the depth of soil penetration of the fragments to evaluate the damage of the rotor catastrophic failure.

Both experimental and analytical works have been done to characterize the earth penetration of a fast traveling object. [40-43] Most of the studies were done with the objective to develop effective earth penetrating weapons. These studies are also valid for analyzing rotor failure, since the fragments of the rotor also travel at similar high speeds.

The equations to be used to predict the penetration path length into a uniform layer or half space of rock, concrete, or solid were given by Young. [44]

$$D = 0.3\, S\, N \left(\frac{W}{A}\right)^{0.7} \ln(1 + 2V^2 10^5) \quad for\ V < 200\ ft/\sec \tag{6.20}$$

$$\mathrm{D} = 0.00178\ \mathrm{S\ N} \left(\frac{\mathrm{W}}{\mathrm{A}}\right)^{0.7} (V - 100) \quad for\ V \geq 200\ ft/\sec \tag{6.21}$$

where D is the penetration distance in feet, S is the penetrability of target. N is the nose performance coefficient. W is the weight of the penetrator in pounds, and V is the impact velocity in feet per second. A is defined as the cross sectional area of the penetrator which is calculated using average body diameter.

The nose shape of the penetrating object also affects the penetration length. As shown is the equation for penetration distance, N is a dimensionless coefficient that characterize the effectiveness of certain nose shapes of the objects. Nose shape performance coefficients were given by Richmond and Young. [44, 45]

$$N = \begin{cases} 0.56 & for\ flat\ nose\ shape \\ 0.18\dfrac{L_n}{d} + 0.56 & for\ ogive\ nose\ shape \\ 0.25\dfrac{L_n}{d} + 0.56 & for\ conic\ nose\ shape \end{cases} \tag{6.22}$$

where L_n is the length of penetrator nose in inch, and d is the diameter of penetrator in inch. For objects with nose shapes other than flat, ogive and conic, the nose shape is approximated with a flat, ogive or conic shape.

The penetrability of target, S-number, in the penetration equation is given:

S-number	**Target Description**
2 - 4	Dense, dry, cemented sand. Dry caliche. Massive gypsite and selenite.
4 - 6	Gravel deposits. Sand, without cementation. Very stiff and dry clay.
6 – 9	Moderately dense to loose and, no cementation, water content not important.
8 - 10	Soil fill material, with the S-number range depending on compaction.

5 - 10	Silt and clay, low to medium moisture content, stiff. Water content dominates penetrability.
10 - 20	Silt and clay, moist to wet. Topsoil, loose to very loose.
20 - 30	Very soft, saturated clay. Very low shear strength.
30 - 60	Clay marine sediments, either currently (Gulf of Mexico) or recent geologically (mud deposits near Wendover, Utah)
> 60	It is likely that the penetration equations do not apply

Table 6.2: Penetrability of targets, S-number. [44]

To obtain an idea of soil penetration of rotor fragment, a simplified model is constructed as shown in Figure 6.6.

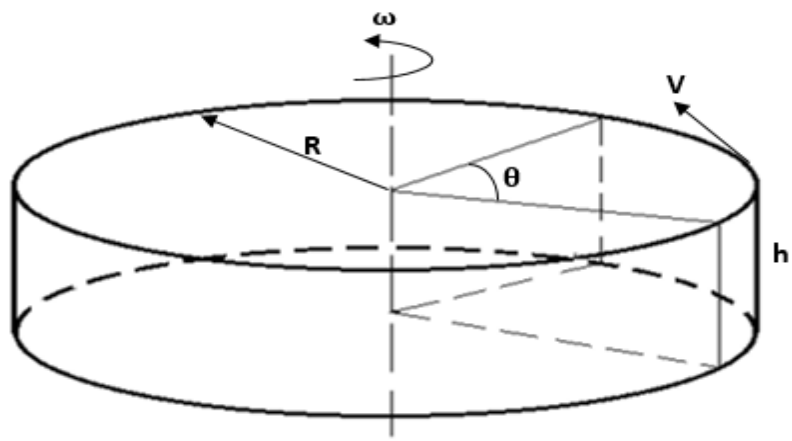

Figure 6.6: Simplified rotor fragment soil penetration model.

Assume a portion of the rotor θ breaks off. The fragments travel with a speed equals to the tip speed of the rotor which is $V = \omega R$. The weight and cross sectional area of the penetrator are calculated respectively by:

$$W = \frac{\theta \rho R^2 h}{2} \tag{6.23}$$

$$A = 2\tan\left(\frac{\theta}{2}\right) Rh \tag{6.24}$$

The nose shape of the fragments is more close to a flat nose, and therefore the nose shape coefficient N equals to 0.56. Since the tip speed of the rotor is usually higher than 200 ft/sec, the penetration length of the rotor fragment can be estimated by:

$$D \cong 0.001\,\mathrm{S}\left(\frac{\theta \rho R}{4\tan\left(\frac{\theta}{2}\right)}\right)^{0.7} (\omega R - 100) \tag{6.25}$$

The combined inaccuracy of predicted penetration length by equations (penetration equation and S-number equation) is about 15% to 20%. [44]

7. Rotor Aerodynamics

The velocity at the tip of the rotor at high rotational speed may exceed the speed of sound under ambient pressure. To increase the energy storage efficiency, the rotor is designed to be contained in a vacuum closure to reduce the drag loss. With a vacuum pump, the air pressure can be maintained at high vacuum level. However, the drag loss still accounts for a big portion of the power loss of the flywheel storage system. In this chapter, an analytical model for calculating drag loss of the rotor is discussed. The model is then compared to the experimental data obtained from a test of 70 inch disc rotor spinning inside a vacuum chamber.

7.1 Analytical Model of Rotor Aerodynamics

To simplify the problem, the rotor is assumed to be a uniform disk of radius R and thickness h and to be contained in a vacuum chamber that is distance d away from the surface of the rotor as shown in Figure 7.1. The rotor spins at an angular velocity ω.

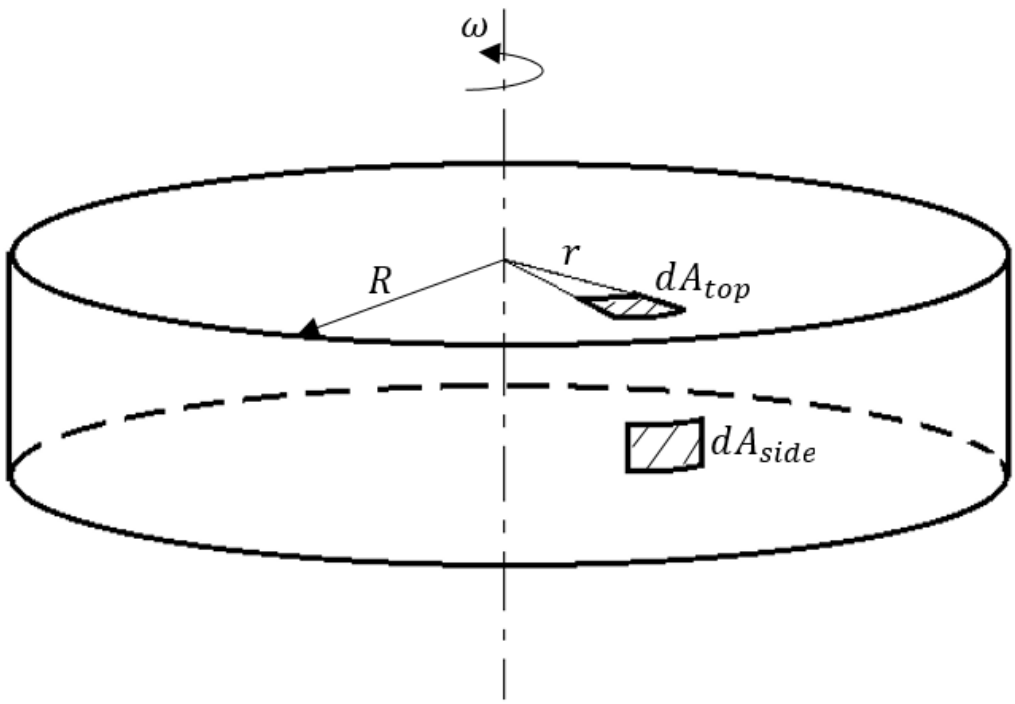

Figure 7.1: Uniform thickness disc rotor model for aerodynamic drag calculation.

In the flywheel energy storage system, the air pressure inside the vacuum chamber is maintained with a vacuum pump to be very low (below 1 mbar), and assume the temperature inside the chamber is kept around room temperature. Under these circumstances, ideal gas law can be used as a suitable model to describe the relation of pressure, temperature and density of air:

$$\frac{P}{\rho} = R_{air}T, \qquad where \quad R_{air} = 287\frac{J}{kgK} \tag{7.1}$$

To determine the type of flow and drag, one has to know the viscosity of air flow on the surface which is a measurement of the flow's resistance to deformation by shear or tensile stress. Viscosity is known to have a strong dependence on temperature and a weak dependence on pressure of the flow. As shown in the Figure 7.2 below, when temperature is fixed, the variance of dynamic viscosity of dry air is insignificant in a small range of pressure from 0 to ambient pressure ($0.101325\ MPa$).

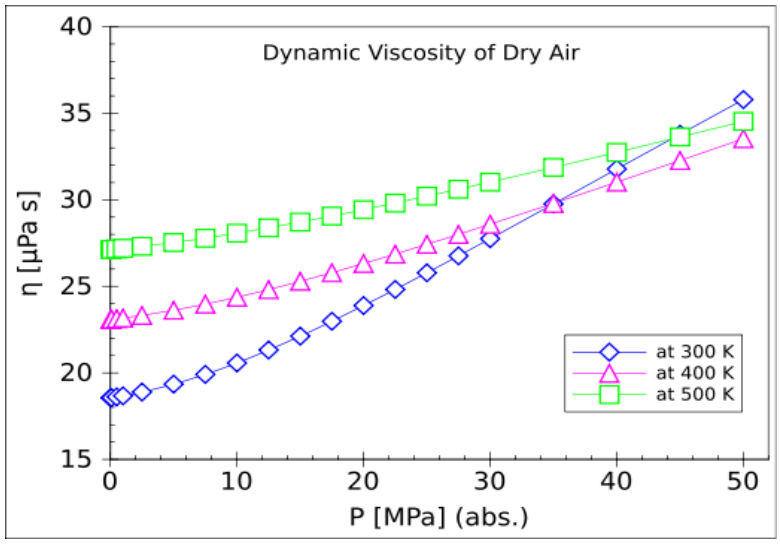

Figure 7.2: Dynamic viscosity of dry air as a function of pressure and temperature. [46]

Therefore, viscosity of air is assumed to be only temperature dependent and is independent on pressure in this model. The viscosity values of air at different temperatures were evaluated experimentally and shown in Figure 7.3.

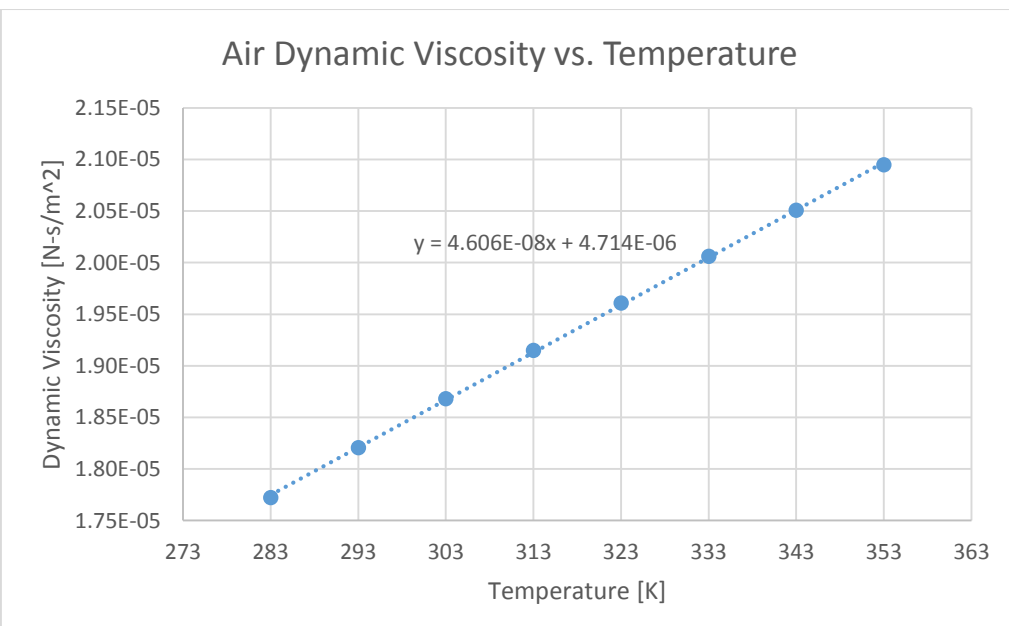

Figure 7.3: Dynamic viscosity of air versus temperature @ ambient pressure.

A linear interpretation of the experimental data gives the relationship between temperature and dynamic viscosity of air.

$$\mu = \text{dynamic viscosity} = 4.61 \times 10^{-8} \cdot T + 4.71 \times 10^{-6} \quad \left[\frac{N \cdot s}{m^2}\right] \tag{7.2}$$

Kinematic viscosity can be calculated as the ratio between the dynamic viscosity and density of the flow:

$$\nu = \text{kinematic viscosity} = \frac{\mu}{\rho} \tag{7.3}$$

Reynold's number is a dimensionless aerodynamic parameter that characterizes the different flow regimes within the flow. For the flywheel system, the rotor is confined in an enclosure that is very close to the surface of the rotor, and is spinning at a very fast speed. Therefore, calculating the Reynold's number of a rotating disk is a challenge. While the typical way of calculating Reynold's number of a free spinning rotor in flow is given by

$$\mathrm{Re} = \frac{vL}{\nu} = \frac{\omega \mathrm{r}^2}{\nu} \tag{7.4}$$

This equation does not account for the effect of the close spaced walls of the vacuum chamber. The flow is restricted by the moving rotor surfaces and the walls.

The transition Reynold's number, Re_{tr}, at which the boundary layer transits from laminar flow to turbulent flow is about 500**.** [47, 48] Therefore, the transition radius over which the boundary layer changes from laminar flow to turbulent flow is:

$$Re_{tr} \approx 500 \tag{7.5}$$

$$\mathrm{r_{tr}} = \sqrt{\frac{Re_{cr}\nu}{\omega}} \tag{7.6}$$

To simplify the calculation of drag, the flow over the region $0 < \mathrm{r} < \mathrm{r_{tr}}$ is defined as laminar flow, and the flow over the region $\mathrm{r_{tr}} < r < R$ is turbulent flow. The actual behavior of the flow in the transition zone between laminar to turbulent flow is more complicated, but for the flywheel application the transition radius is small enough that most of the flow is turbulent, and the laminar flow only contributes a negligible portion to the overall drag loss of the rotor, which will be shown in the calculation later. The top, bottom and side surfaces of the rotor can be divided into infinite small flat surfaces with area dA. The total drag is calculated by integrate the drag on all the infinite surfaces. The drag coefficient of a flat plate parallel to the flow direction for laminar flow, $\mathrm{C_{d_l}}$, was given by Blasius. [49] The drag coefficient for turbulent flow, $\mathrm{C_{d_t}}$, was given by von Kármán. [50]

$$\mathrm{C_{d_l}} = \frac{0.664}{(Re)^{0.5}} \quad for\ laminar\ flow \tag{7.7}$$

$$C_{d_t} = \frac{0.0534}{(Re)^{0.2}} \quad for\ turbulent\ flow \tag{7.8}$$

Drag force experienced by a plate with area A moving through the flow can be obtained by:

$$D = \int \frac{1}{2}\rho V^2 C_d dA \tag{7.9}$$

The above equation evaluates the drag force generated on both sides of the plate. For the rotor model, the drag force on each infinitesimal plate is only on one side, and therefore the force should be half. The drag force on the top surface of the rotor can be calculated by integrating the drag force on all infinitesimal plates.

$$D_{top} = \frac{D}{2} = \int \frac{1}{4}\rho V^2 C_d dA \tag{7.10}$$

The drag force on the entire rotor can be evaluated by summing the drag forces on top, bottom and side surfaces.

$$D_{top} = \int_0^{r_{cr}} \frac{1}{4}\rho V^2 C_{d_l} dA + \int_{r_{cr}}^{R} \frac{1}{4}\rho V^2 C_{d_t} dA \tag{7.11}$$

$$D_{top} = D_{bottom} = \int_0^{r_{cr}} \frac{1}{4}\rho(\omega r)^2 \frac{0.664}{\left(\frac{\omega r^2}{\nu}\right)^{0.5}} (2\pi r)\, dr + \int_{r_{cr}}^{R} \frac{1}{4}\rho(\omega r)^2 \frac{0.0534}{\left(\frac{\omega r^2}{\nu}\right)^{0.2}} (2\pi r)\, dr \tag{7.12}$$

$$D_{side} = \frac{1}{4}\rho(\omega R)^2 C_{d_t}(2\pi R h) \tag{7.13}$$

$$D_{total} = D_{top} + D_{bottom} + D_{side} \tag{7.14}$$

The total moment applied on the rotor due to air drag is calculated by integrating the amount of drag moment generated by all the infinitesimal plates and summing the moments generated on all the surfaces of the rotor:

$$dM = r \times dD \tag{7.15}$$

$$M_{top} = M_{bottom} = \int_0^{r_{cr}} r \times \frac{1}{2}\rho V^2 C_{d_l} dA + \int_{r_{cr}}^{R} r \times \frac{1}{2}\rho V^2 C_{d_t} dA \tag{7.16}$$

$$M_{side} = R \times \frac{1}{2}\rho(\omega R)^2 C_{d_t}(2\pi R h) \tag{7.17}$$

$$M_{total} = M_{top} + M_{bottom} + M_{side} \tag{7.18}$$

Then, the loss of power due to the aerodynamic drag is given by:

$$P_{drag} = D \cdot V = \int dD \cdot (\omega r) = M \cdot \omega \tag{7.19}$$

The loss of power due to air drag is a function of temperature and pressure of the air inside the chamber as well as the rotational speed of the rotor. Figure 7.4 – 7.6 show the dependence of the aerodynamic drag power loss on temperature, pressure and rotational speed. The figures were generated for a 70 inch diameter and 10 inch thick disc rotor spinning inside a vacuum chamber.

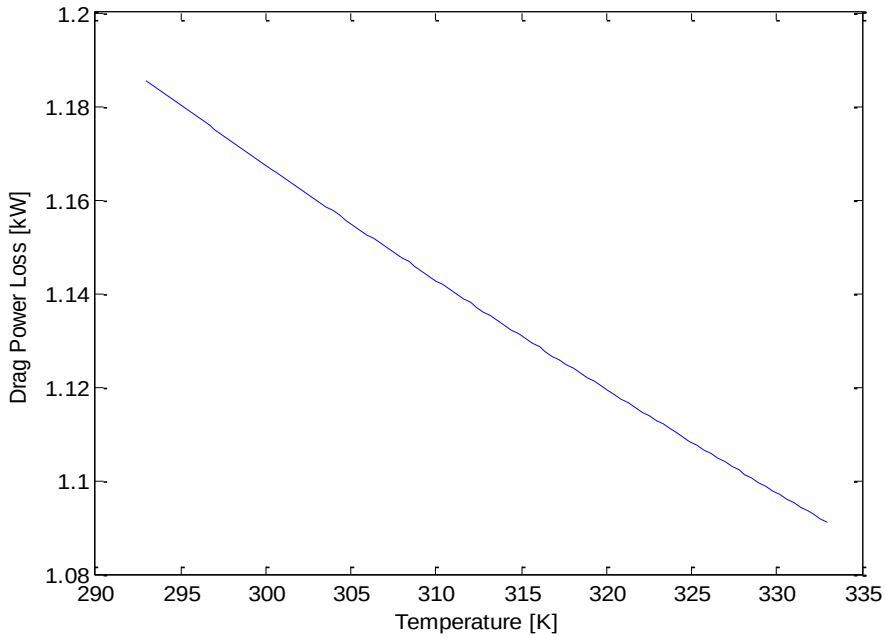

Figure 7.4: Relation between power loss due to aerodynamic drag and temperature of the air flow.

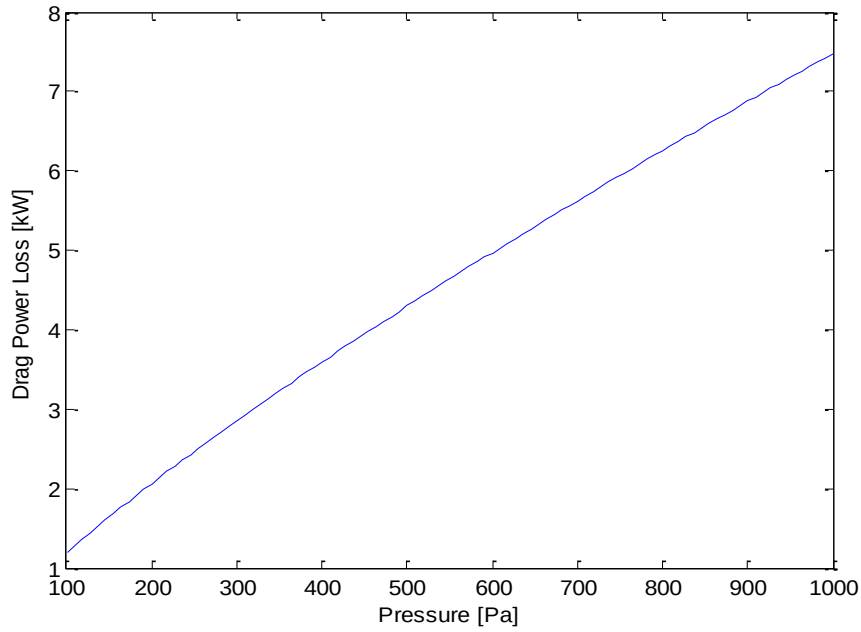

Figure 7.5: Relation between power loss due to aerodynamic drag and pressure inside the vacuum chamber.

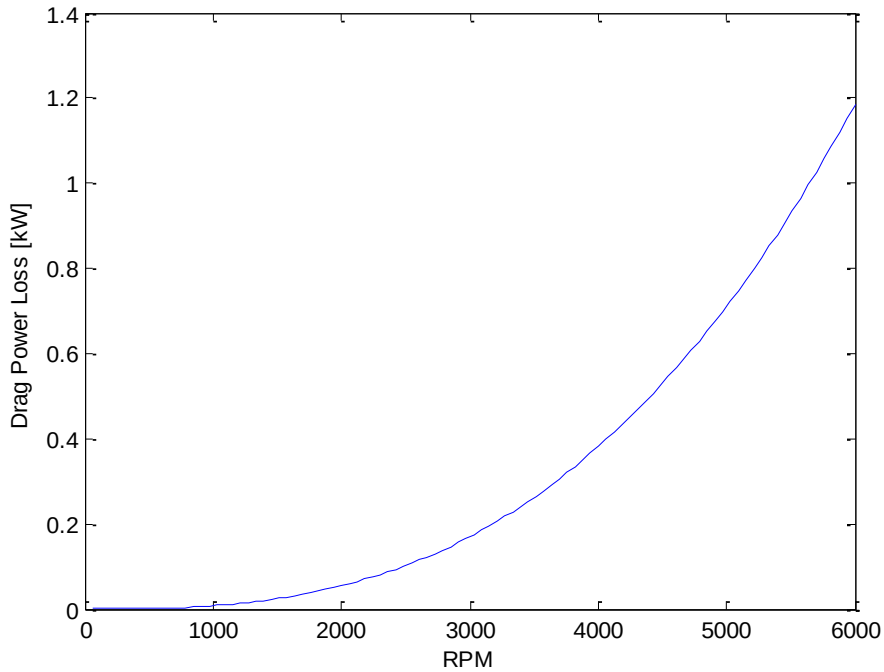

Figure 7.6: Relation between power loss due to aerodynamic drag and rotational speed.

The above figures give a parametric view of power loss of the rotor due to aerodynamic drag. The drag loss has a strong dependence on the pressure of the flow inside the vacuum chamber, and has a week dependence on temperature change of the flow. The drag loss is also proportional to the square of rotational speed of the rotor.

7.2 Experimental Validation

A 70 inch diameter and 10 inch thick steel disc rotor was contained inside a vacuum chamber. The rotor was spun up to 6000 RPM.

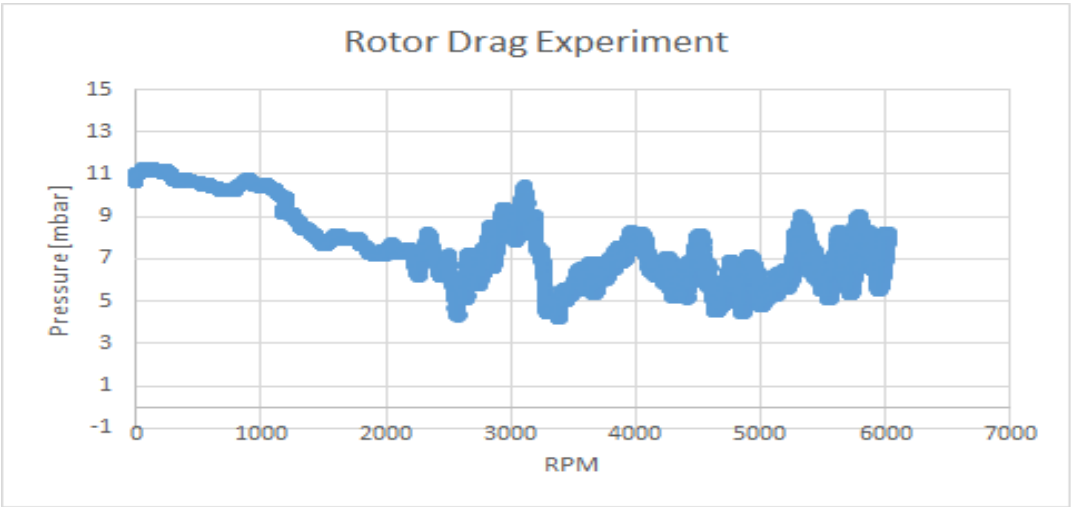

Figure 7.7: Pressure versus rotor rotational speed in the drag power loss experiment.

The pressure inside the pressure chamber was controlled by a vacuum pump and measured with a vacuum sensor. Due to the leakage of the system and the limitation of the vacuum pump, the pressure in the chamber was keep around 7 mbar with a varying range between 4 mbar to 11 mbar. The pressure data and the rotational speed of the rotor is plotted in Figure 7.7.

The total power loss of the system consisted of power loss of the bearing, rotary vacuum seals and electric motor. Power loss due to drag was calculated by subtracting the contribution of the bearing, vacuum seals and electric motor power loss. The theoretical model of drag power loss calculation of the rotor spinning under 7 mbar vacuum pressure is compared to the experimental data in Figure 7.8. The power loss from the experimental data is higher than the theoretical model especially from 0 to 3000 rpm which is due to the fact that the actual pressure inside the chamber was higher than 7 mbar.

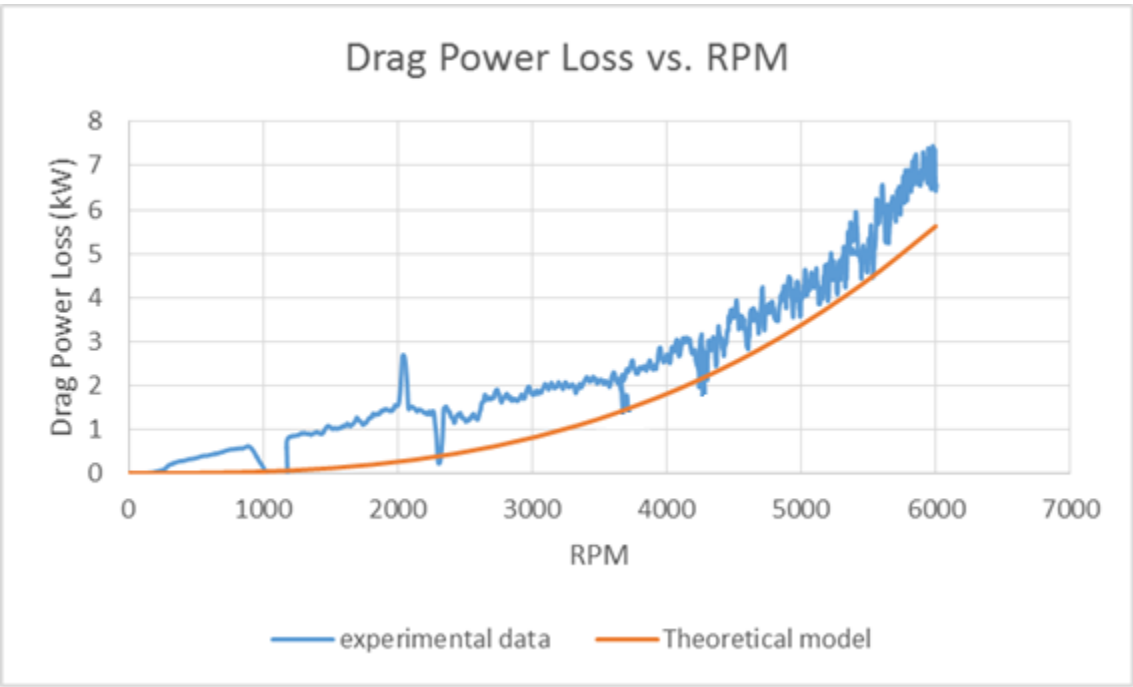

Figure 7.8: Comparison of experimental data and theoretical model of aerodynamic drag power loss of disc rotor inside a vacuum chamber.

8. Sub-System Design and Analysis

Sub-system of flywheel energy storage system is defined as everything other than the rotor. It includes bearings, vacuum system, cooling system, motor and transmissions and etc. Design of the sub-system is as critical as the rotor. The steel rotor has large weight and rotates at very high speed, and therefore puts challenge in designing the bearings. The bearings take both the axial load due to the weight of the rotor and radial load due to the gyroscopic moment. In order to reduce the power loss due to aerodynamic drag to an acceptable level, it is essential for the flywheel to operate in vacuum. O-ring type stationary vacuum seals as wells as rotary seals are necessary to keep the vacuum level low. In addition, the enclosure for the rotor not only needs to have high structural stiffness but also has to act as a vacuum chamber. The sub-system components create power loss. The performance of these components determines the energy storage efficiency and maintenance of the flywheel system. This chapter demonstrates the design and analysis of bearings and vacuum systems.

8.1 Bearing

The bearings in flywheel system are usually under the axial loads due to the weight of the rotor, radial load due to gyroscopic moment of the rotor, in some cases by the forces due to the transmission units and also by dynamic loads. As the combination of high loads and high speeds is often present, the design of bearings for large capacity flywheel energy storage is a challenge. At the same time, the needs to minimize the power loss and extend the life of the bearings make the problem more complicated.

8.1.1 Bearing Types and Material Selection

There are several types of bearings that can be associated with flywheel energy storage systems: deep groove ball bearings, angular contact ball bearings, thrust bearings and magnetic bearings. The selection of the bearings depends on the performance requirements and operating limitations of the system.

Deep groove ball bearings have full shoulders on both sides of the raceways of the inner and outer rings. They can accept radial loads, thrust loads in either direction, or a combination of loads. The full shoulders and the cages used in deep groove bearings make them suitable for the addition of closures.

Angular contact bearings have one ring shoulder removed, either from the inner or outer ring. This allows a larger ball complement than in comparable deep groove bearings, which gives a greater load capacity. Speed capacity of angular contact bearings is also greater. Angular contact bearings can have a contact angle typically ranging from 10° to 25°. Angular contact bearings support combinations of radial and thrust loading. However, they are not suitable to accept radial loads alone. A thrust load of sufficient magnitude must be applied to prevent the bearings from skidding. A single angular contact bearing can be loaded in one thrust direction only which can be an operating load or pre-load.

Magnetic bearings support moving parts without physical contact. Instead, they rely on magnetic fields to bear the loads. However, to keep the magnetic fields. they require continuous power input

to keep the load stable, and thus requiring a back-up bearing in case of power or control system failure. Magnetic bearings have very low friction and the ability to run without lubrication or in a vacuum.

Performance of the bearings depends on the material selections, manufacturing precision, size, configurations and so on. The comparison of performance characteristics of several types of bearings is shown in Table 8.1. Ball bearings consist of inner and outer races, ball containing cage and the balls. Races of bearings are usually made out of chrome steel. The cage materials can be polyamide 66 (PA66), polyetheretherketone (PEEK), brass or others. Metal cages usually have higher temperature ratings than polymer or composite cages. The balls can be made out of steel or ceramics such as SiC. Compared to steel balls, ceramics balls have higher load capacity and impact tolerance.

	Radial Load	**Axial Load**	**Speed**	**Power loss**
Deep groove bearings	Good	Normal	High	Very low
Angular contact bearings	Good	Good	High	Low
Thrust bearings	limited	Very good	Low	Low
Magnetic bearings	Good	Good	High	High

Table 8.1: Bearing types and comparison of performance of different types of bearings with regard to load, speed and power loss.

8.1.2 Bearing Design Configuration

Angular contact bearings especially can be installed in pre-loaded duplex sets, back to back (DB) or face to face (DF) for supporting axial loads in both directions or in tandem (DT) for additional load capacity. Both back to back and face to face configurations add stability to the shaft. Tandem configuration is usually designed to double the axial load capacity to support the heavy weight of the rotor.

8.1.3 Bearing Lifetime Calculation

The lifetime of a ball bearing considered in engineering designs is usually limited by the onset of fatigue, plastic deformation or the balls or spalling of the raceways, ball containing case and balls, assuming the bearing was properly selected and installed, effectively lubricated and protected against contaminants. When a bearing no longer fulfills its minimum performance requirements in terms of torque, vibration or elastic yield, its service life is considered to be ended. If the bearing remains in operation, its performance is likely to decline until the failure of the bearing. In this case, bearing performance is properly used as the measuring stick in determining bearing life.

The traditional basic relationship between bearing load capacities with fatigue life is presented as:

$$L_{10} = \left(\frac{C}{P}\right)^3 \times 10^6 \quad [revolutions] \tag{8.1}$$

L_{10} is minimum life in revolutions for 90% survival rate of a typical group of identical bearings. C is the basic dynamic load rating of the bearing. P is equivalent radial load given by:

$$P = XR + YT \tag{8.2}$$

$$or \quad P = R \quad whichever\ is\ greater \tag{8.3}$$

R is radial load. T is thrust load. X is radial load factor relating to contact angle. Y is axial load factor depending upon contact angle. These factors can be found in Appendix C.

To better understanding of the causes of fatigue, the life calculation equation is modified to:

$$L_{10_{mod}} = A_1 A_2 A_3 L_{10} \tag{8.4}$$

A_1 is statistical life reliability factor for a chosen survival rate. A_2 is life modifying factor reflecting bearing material type and condition. A_3 is application factor. Values of A_1, A_2, A_3 can be find in Appendix C according to the bearing type and operating conditions. [51]

8.2 Vacuum & Seal

To achieve the vacuum level and reduce the drag on the rotor, vacuum pump is commonly equipped in flywheel energy storage system. The vacuum level inside the vacuum chamber affects the energy storage efficiency. When there is no leakage and outgassing of the vacuum chamber, the relationship between the pressure inside the vacuum chamber p and time t can be described in the following equation.

$$\frac{dp}{dt} = -\frac{S}{V}p \tag{8.5}$$

$$lnp = lnp_o - \frac{S}{V}t, \quad where\ p_o = p|_{@t=0} \tag{8.6}$$

where S is the pump speed, V is the air volume inside the chamber. This relationship can be used to size the vacuum pump. [52]

8.2.1 Outgassing

Gas is absorbed on the surface while they are at atmospheric pressure and then desorbed slowly when they are under vacuum. The rate of desorption will depend on the binding energies of the various gases to the surface, the surface temperature, and the surface coverage.

$$\frac{dn}{dt} = -Kf'(\theta)\, exp\left(-\frac{E_d}{RT}\right) \tag{8.7}$$

where K is a constant, $f'(\theta)$ is a function of surface coverage, E_d is the desorption activation energy, R is the gas constant, and T is the temperature. [52]

Some gas or liquid is dissolved in the material during manufacture, and slowly diffuses out under vacuum. The outgassing due to this mechanism depends on the nature of the material, its temperature, the solubility of the gas, and its rate of diffusion. The solution to relate diffusion to outgassing rate of unit area is given by Lewin [53]:

$$c(x,t) = C_0 erf[x/2(Dt)^{\frac{1}{2}}] \tag{8.8}$$

$$q = D\left(\frac{\partial c}{\partial x}\right)_{x=0} = C_0 D^{1/2}(\pi t)^{-1/2} \tag{8.9}$$

In addition, gas may be evolved after permeating through the walls of the vacuum chamber and seals. This mechanism depends on the nature of the material and on the thickness of the part. Plastics and rubbers usually have higher permeation rate that metals and therefore are not recommended for high vacuum level. Outgassing rates of some commonly used materials in vacuum systems are listed in Table 8.2.

Materials	**Outgassing Rate @ room temperature** $\mathbf{torr \cdot liter \cdot sec^{-1} \cdot cm^{-2}}$
AL 6061 T4	1×10^{-14}
Copper	2.3×10^{-6}
Stainless Steel 304	$5 \times 10^{-12} - 1.5 \times 10^{-9}$
Viton	5×10^{-11}
Teflon	$7.5 \times 10^{-6} - 1.5 \times 10^{-7}$

Table 8.2: Outgassing rates of possibly used materials for vacuum system in flywheel energy storage system at room temperature. [54]

8.2.2 Vacuum Pump

Vacuum pumps can be categorized by their ultimate vacuum level. There are four typical vacuum/pressure regimes for vacuum pumps:

Pressure Regime	**Vacuum Level (torr)**
coarse vacuum	760 – 1
rough vacuum	1 - 10^{-3}
high vacuum	10^{-4} - 10^{-8}
ultra-high vacuum	10^{-9} – 10^{-12}

Table 8.3: Typical vacuum/pressure regimes of vacuum pumps.

For each pressure regime, there are several vacuum technologies that could achieve the vacuum level. The commonly used types of vacuum pumps are rotary vane pump, scroll pump, diaphragm pump, piston pump, and turbo pump. Rotary vane pump is usually used as a roughing pump. It has the advantages such as cheaper cost and relatively large flow rate. However, it is an oil based type of pump, and therefore will emit oil vapor. Oil recirculation system is often equipped with the rotary vane pump to trap oil vapor and recirculate into the oil reservoir. Regular maintenance such as adding oil and changing oil filter is required for this type of pump. Scroll pump is similar to rotary vane pump in terms of ultimate vacuum level and flow rate. It is an oil-free dry pump which does not require oil recirculation. However, the scroll o-ring also need regular maintenance to keep the ultimate vacuum level. Diaphragm pump is also a dry pump which is often used in laboratory environments. The advantages of diaphragm pumps are that they are oil free and are very quiet. The disadvantage of diaphragm pump is its limited flow rate. When high vacuum level is required in some flywheel energy storage system, piston pump or turbo pump can be considered as a second

stage pump. They can reach very low vacuum level below the rough vacuum level and have large flow rate.

8.2.3 Seals

Vacuum seal is a critical part of the vacuum system. The selection of the seals often determines the ultimate vacuum level of the system. For flywheel energy storage system, rubber O-ring type seals, vacuum flanges with metal gaskets, and NPT male and female threads with Teflon tape are the three common choices. Rubber O-ring seals are made of polymers such as Buna-N and Viton They are typically used for systems with vacuum levels higher than high vacuum regime because of the permeability of the materials and surface contact limitation. The contact surfaces are machined to have a surface roughness below 32 rms. For pressure below high vacuum regime, stainless steel ConFlat (CF) vacuum flanges and metal gaskets are often selected. The gaskets can be made of copper, nickel or aluminum depending on the applications.

9. Conclusion and Future Work

9.1 Conclusion

This dissertation demonstrated the fundamental design work for a large scale flywheel energy storage system that can be integrated with the current electrical grid system and clean energy smart grids. Design of the rotor is emphasized since rotor is the most critical component of the flywheel energy storage system, and catastrophic failure of the rotor needs to be prevented by a safe design. The overall work can be divided into four phases: 1) theoretical analysis and conceptual design; 2) material testing; 3) stress and fracture mechanics analysis; 4) energy storage efficiency evaluation and sub-system design.

Theoretical analysis of the rotor gives a parametric view of the rotor design. Stress-strain distribution within the rotor is related with the operating rotational speed, rotor geometry, material properties, energy density, and so on. The purpose of the theoretical analysis is to convert all the design requirements into a conceptual design of the whole flywheel energy storage system. Analysis of both steel rotor and composite rotor shows the difference in stress-strain distribution and failure mechanisms between the two kinds of rotors. For large capacity energy storage, steel rotor is preferred over composite rotor considering the capacity and cost of the system. A disc rotor is used as a representing baseline design of the rotor to be used in the conceptual design.

Material testing on the rotor material provides mechanical properties of the material which can be used in design and analysis of the rotor. Three mechanical tests were conducted: tensile test, fracture toughness test, and fatigue crack propagation test. Material test specimens were machined out of a testing block of the same material as the rotor. The results of the tensile tests gave the elastic modulus, yield strength, ultimate tensile strength, and elongation of the rotor material, which were later applied in the theoretical and finite element analysis. Fracture toughness test on compact tension specimens measured the critical J-integral value and critical stress intensity factor which were used in fracture mechanics calculations to predict rotor lifetime. Fatigue crack propagation tests gave the relationship between crack growth rate and the loading conditions. The result was fitted to a mathematical model to characterize the behavior of defects or cracks in the rotor and estimate the lifetime cycles of the rotor.

Finite element analysis of the rotor showed the static and dynamic response of the rotor under load. The FEA models were built in Abaqus CAE. First, the effects of heat treatment of the rotor were obtained by a transient heat transfer FEA model. Stress-strain distribution within the rotor was calculated for varying temperatures. Stress and strain were not uniformly distributed within the rotor because of the difference in cooling speed and temperature distribution. Residual stress was induced in the heat treatment process and was calculated in the FEA model. The model showed that the residual stress appears roughly 1 inch thick layer on the surface of the rotor. Stress-strain distribution was obtained under static rotational body force. This static FEA model can be used to evaluate the rotor geometric design and determine the maximum operational rotational speed. Optimizing the geometry of the rotor can reduce stress concentration and lower the overall stress state. Both 2D and 3D FEA models of the rotor showed consistent results of stress. Dynamic FEA model of the rotor estimated the resonant models and frequencies of the rotor and other structures

to make sure the resonant frequencies are above the maximum rotational speed. The results of the FEA models were fed back to the fracture mechanics analysis to calculate the critical crack length of the material. Initial crack length can be assumed to be the minimal detectable flaw size of ultrasonic flaw detection which is determined by the frequency of the transducer and the properties of rotor material. Initial crack length and critical crack length were then plugged into the fatigue crack propagation model to calculate the lifetime expectancy of the rotor.

Finally, energy storage efficiency of the flywheel energy storage system was considered. To be applicable as an energy storage solution for the electric grid, the flywheel system needs to have high efficiency and low power loss. The power loss is due to electric motor loss, aerodynamic drag on the rotor, and sub-system components include bearings and vacuum system. Theoretical aerodynamic model of a rotating disc inside a containment was discussed. The model was then compared to experimental data of a large steel rotor rotating in a vacuum chamber. As shown, the drag power loss is linear to the pressure inside the chamber and to the square of the rotating speed. Temperature change has less significant effect on the power loss. Life expectancy and maintenance of the flywheel energy storage system is also determined by the lifetime of subsystem components. The design of bearing system with proper bearing selection and configuration can increase the bearing life and reduce power loss. In order to reduce the aerodynamic drag, vacuum system design were looked at including the effect of outgassing of the vacuum chamber, vacuum seal selection, and vacuum pump selection.

9.2 Future Work

Future work on large scale flywheel energy storage system will continue to focus on characterizing the rotor to prevent catastrophic failure and also increasing energy storage efficiency on system level. There are several topics that can be further studied in order to improve the robustness and gain more understanding of the design:

1. Molecular FEA model of heat treatment: The finite element model of the residual stress in the rotor due to the heat treatment process has the assumption that the molecular structure of the rotor material is homogeneous. However during the quenching process, the sudden temperature change causes non-uniform cooling rate within the rotor which results in different microscopic structures between the surface and the center of the rotor. This phenomena was not modeled in the finite element model and can lead to inaccurate results in residual stress calculation. A molecular level finite element analysis is needed to model the microscopic structure variance due to the heat treatment, which will lead to better understanding of residual stress distribution and magnitude within the rotor.
2. Genetic algorithm to optimize the flywheel shape vs. stress level vs. energy density: Genetic algorithm can be integrated with the finite element analysis to optimize the flywheel geometry in order to reduce the stress level but as the same time achieve the highest energy density. The simple disc rotor can be used as a baseline model for the genetic algorithm. This work will require large amounts of computing power which may need the assist of supercomputers.
3. S-N experimental data: Although fatigue crack propagation model provides a conservative way to estimate the lifetime of the rotor, it is necessary to evaluate the life cycles of the

rotor versus the applied stress or maximum rotational speed. Smaller scale rotors made out of the same rotor material can be used as the test specimens. The experiments will require several small rotors cycling between zero to different maximum speeds. The S-N curve can be generate using the maximum speed vs. life cycles data. A simpler approach will be using tensile test samples of the rotor material on cyclic tensile tests to generate a representing S-N curve of the rotor.

4. Development of in-situ rotor health monitoring system: An in-situ rotor health monitoring system can detect real-time damages inside the rotor to alert the operator before catastrophic failure. One way to accomplish this is to use ultrasonic flaw detection. An ultrasonic transducer can be attached to a robotic arm built inside the vacuum chamber. The arm is controlled to push the transducer to the surface of the rotor when rotor is static and detect flaws/cracks that are larger than the minimal detectable crack size.

APPENDIX A: Drawing of Material Tensile Test Sample

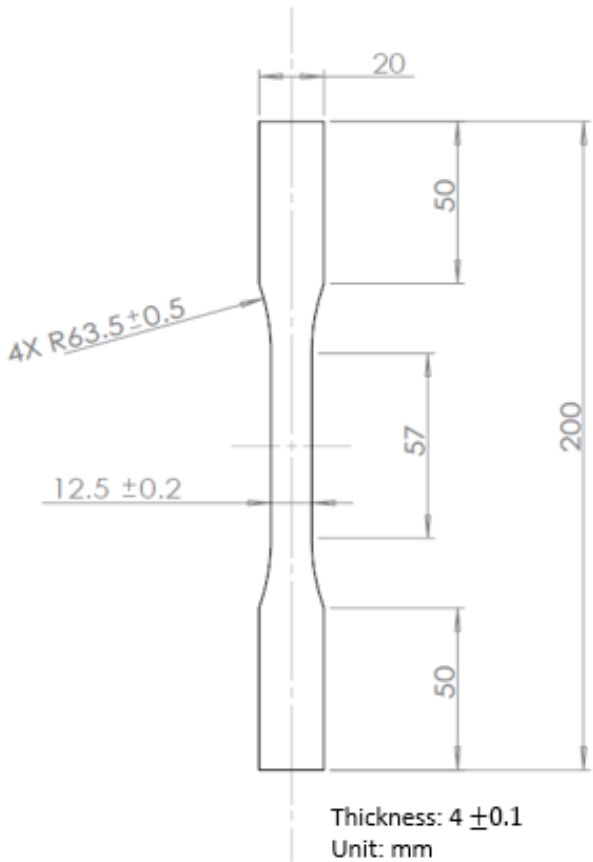

Figure A.1: Drawing of dog bone tensile test sample according to requirements in ASTM standard E8.

APPENDIX B: Fracture Toughness & Fatigue Crack Propagation Tests

The drawing of the compact tension specimens for fracture toughness test and fatigue crack propagation test.

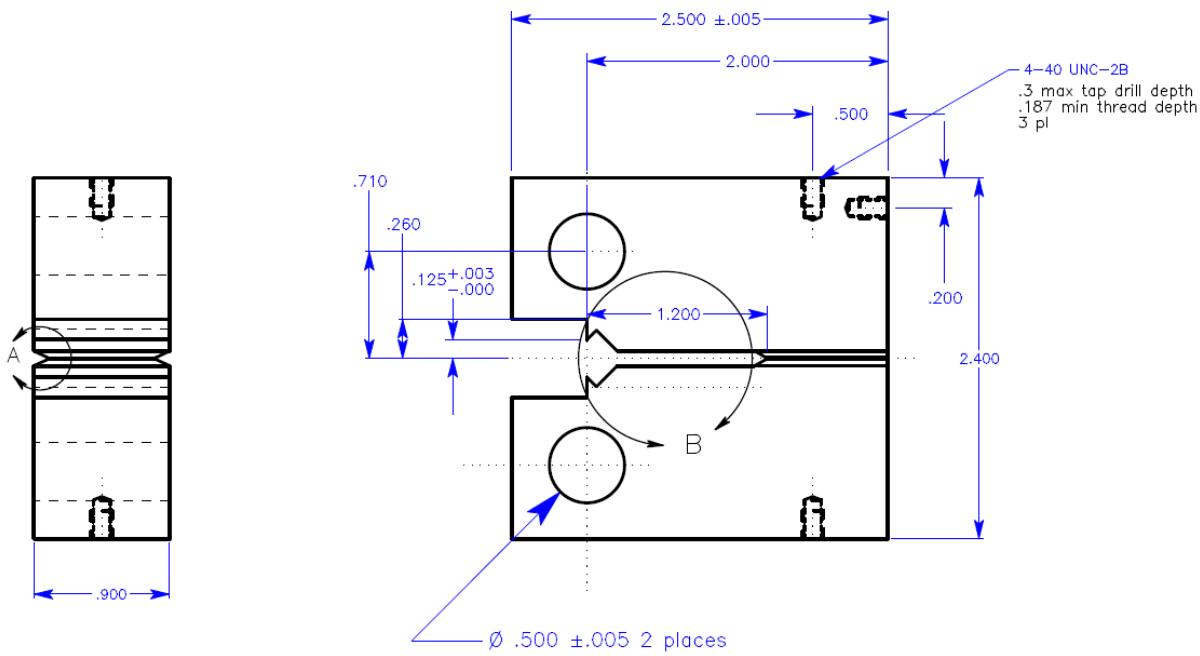

Figure B.1: Fracture toughness test C(T) sample drawing.

Experiment setup of the fracture toughness test:

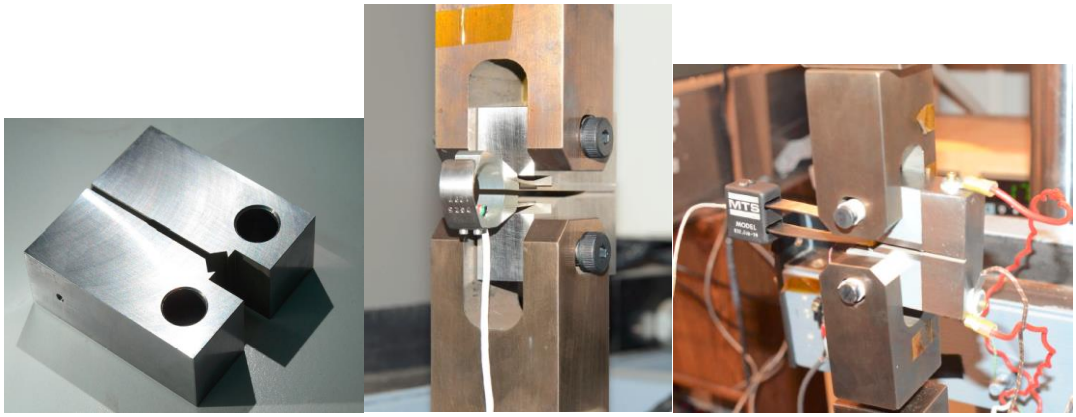

Figure B.2: Fracture toughness test sample and test setup.

Figure B.3: Crack surface of a C(T) sample after fatigue crack propagation test.

APPENDIX C: Parameters for Bearing Life Calculation

Load factors, X and Y for instrument bearings: [51]

T/nd^2	Contact Angle [degrees]			
	5	**10**	**15**	**20**
	Values of Axial Load Factor, Y			
100	3.30	2.25	1.60	1.18
200	2.82	2.11	1.56	1.18
400	2.46	1.95	1.52	1.18
600	2.26	1.85	1.47	1.18
800	2.14	1.78	1.44	1.18
1200	1.96	1.68	1.39	1.18
2000	1.75	1.55	1.32	1.18
3000	1.59	1.45	1.27	1.18
4500	1.42	1.34	1.21	1.18
	Values of Radial Load Factor, X			
	0.56	0.46	0.44	0.43

Table C.1: Axial load factor Y and radial load factor X for angular contact instrument bearings. (n is the number of balls, and d is bore diameter of the bearings.)

T/nd^2	Contact Angle [degrees]				
	5	**10**	**15**	**20**	**25**
	Values of Axial Load Factor, Y				
50	-	2.10	1.55	1.00	0.87
100	2.35	1.90	1.49	1.00	0.87
150	2.16	1.80	1.45	1.00	0.87
200	2.03	1.73	1.41	1.00	0.87
250	1.94	1.67	1.38	1.00	0.87
300	1.86	1.62	1.36	1.00	0.87
350	1.80	1.58	1.34	1.00	0.87
400	1.75	1.55	1.31	1.00	0.87
450	1.70	1.52	1.30	1.00	0.87
500	1.67	1.49	1.28	1.00	0.87
750	1.50	1.38	1.21	1.00	0.87
1000	1.41	1.31	1.17	1.00	0.87
1500	1.27	1.20	1.10	1.00	0.87
2000	1.18	1.13	1.05	1.00	0.87
2500	1.12	1.06	1.00	1.00	0.87
3000	1.07	1.02	1.00	1.00	0.87
3500	1.03	1.00	1.00	1.00	0.87
4000	1.00	1.00	1.00	1.00	0.87
4500	1.00	1.00	1.00	1.00	0.87
	Values of Radial Load Factor, X				
	0.56	0.46	0.44	0.43	0.41

Table C.2: Axial load factor Y and radial load factor X for angular contact spindle and turbine bearings. (n is the number of balls, and d is bore diameter of the bearings.)

Factors for modified bearing life calculation: [51]

Survival Rate (%)	Bearing life notation	Reliability factor, A_1
90	L_{10}	1.00
95	L_5	0.62
96	L_4	0.53
97	L_3	0.44
98	L_2	0.33
99	L_1	0.21

Table C.3: Reliability factor A_1 for various survival rates of bearings.

Race Material / Process	440C	52100	M50	Cronidur 30°
Air Melt	.25X	NA	NA	NA
Vacuum processed	NA	1.0	NA	NA
VAR (CEVM)	1.25X	1.5X	NA	NA
VIM-VAR	1.5X	1.75X	2.0X	NA
PESR	NA	NA	NA	4.0X

Table C.4: Life modifying factor A_2 for bearing life calcualtion.

$$A_3 = \begin{cases} 4.0 \times 10^{-10} nCNUC_p, & for\ miniature\ and\ instrument\ bearings \\ 8.27 \times 10^{-11} nCNUC_p, & for\ spindle\ and\ turbine\ bearings \\ 3, & for\ good\ lubrication \end{cases} \qquad (C1)$$

References

1. Dunn, B., H. Kamath, and J.-M. Tarascon. *"Electrical Energy Storage for The Grid: A Battery Of Choices"*. Science 334.6058 (2011): 928-935.
2. Gyuk, I. et al. *"The United States of Storage - Electric Energy Storage"*. IEEE Power and Energy Magazine 3.2 (2005): 31-39.
3. "*Basic research needs for electrical energy storage*", Office of Basic Energy Sciences, U.S. Department of Energy, Washington, DC, July 2007.
4. "*Electrical Energy Storage Technology Options*", (Report 1020676, Electric Power Research Institute, Palo Alto, CA, December 2010.
5. Soloveichik, G. L. "*Battery Technologies for Large-Scale Stationary Energy Storage*", Annual Review of Chemical and Biomolecular Engineering 2.1 (2011): 503-527.
6. Anderson, M.D., and Carr, D.S., "*Battery Energy Storage Technologies*", Proceedings of the IEEE 81.3 (1993): 475-479.
7. Lachs, W., Sutanto, D., "*Application of Battery Energy Storage in Power Systems*", Proceedings of the International Conference on Power Electronics and Drive Systems, 2, February 21–24, (1995), pp. 700–705.
8. Miller, N., Zrebiec, R., Delmerico, R., Hunt, G., "*Battery Energy Storage Systems for Electric Utility, Industrial and Commercial Applications*", Proceedings of the Eleventh Annual Battery Conference on Applications and Advances, January 9–12, (1996), pp. 235–240.
9. Joseph, A., Shahidehpour, M., "*Battery Energy Storage Systems in Electric Power Systems*", IEEE (2006) 1–8.
10. Hadjipaschalis, I., Poullikkas, A., and Efthimiou, V., "*Overview of Current And Future Energy Storage Technologies For Electric Power Applications*", Renewable and Sustainable Energy Reviews 13.6-7 (2009): 1513-1522.
11. Ibrahim, H., Ilinca A., and Perron J., "*Energy Storage Systems - Characteristics and Comparisons*", Renewable and Sustainable Energy Reviews 12.5 (2008): 1221-1250.
12. Singer, C., and Williams T. I., "*A History of Technology*". Oxford: Clarendon Press, 1954.
13. Beaconpower.com, *"Beacon Power"*. N.p., 2015.
14. www.activepower.com, "*Active Power*". N.p., 2015.
15. Björn, B., Bernhoff, H., and Leijon, M., "*Flywheel Energy and Power Storage Systems*". Renewable and Sustainable Energy Reviews 11.2 (2007): 235-258.
16. Chen, H., Cong, T. N., Yang, W., Tan, C., Li, Y., and Ding, Y., "*Progress in Electrical Energy Storage System: A Critical Review*". Progress in Natural Science 19.3 (2009): 291-312.
17. Díaz-González, Francisco et al. "*A Review of Energy Storage Technologies for Wind Power Applications*", Renewable and Sustainable Energy Reviews 16.4 (2012): 2154-2171.
18. Van Den Avyle, James A., John A. Brooks, and Adam C. Powell. "*Reducing Defects in Remelting Processes For High-Performance Alloys*", JOM 50.3 (1998): 22-25.
19. Park, Soo-Jin. "*Carbon Fibers*", Springer Series in Material Science, Volume 210 2015.
20. Strong, A. Brent., "*Fundamentals of Composites Manufacturing*", Dearborn, MI: Society of Manufacturing Engineers, 2008.
21. Wells, A., "*Unstable Crack Propagation in Metals: Cleavage and Fast fracture*". Proceedings of the Crack Propagation Symposium, Vol. 1, Paper 84. 1961.

22. Rice, J., "*A Path Independent Integral and the Approximate Analysis of Strain Concentration by Notches and Cracks*". Journal of Applied Mechanics, pp. 379-386. 1968.
23. Liu, S.-Y., Chen, I. W., "*Fatigue of Yttria-Stabilized Zirconia – I. Fatigue Damage, Fracture Origins and Lifetime PSrediction*", Journal of the American Ceramic Society 74, 1197–1205. 1991
24. Dauskardt, R.H., James, M.R., Porter, J.R. and Ritchie, R.O., "*Cyclic Fatigue-Crack Growth in SiC-Whisker Reinforced Alumina Ceramic Composite: Long and small-crack behavior"*, Journal of the American Ceramic Society 75, 759–771. 1992.
25. Lai, G. Y. et al. "*The Effect of Austenitizing Temperature on the Microstructure And Mechanical Properties Of As-Quenched 4340 Steel*", Metallurgical Transactions 5.7 (1974): 1663-1670.
26. Zhirafar, S., Rezaeian, A., and Pugh, M., "*Effect of Cryogenic Treatment On The Mechanical Properties Of 4340 Steel*", Journal of Materials Processing Technology 186.1-3 (2007): 298-303.
27. Herring, D., Hill, R., "*Heat Treating*", Materials Park, Ohio: ASM International, 2005.
28. Price, R. F., and Fletcher A. J., "*Determination of Surface Heat-Transfer Coefficients During Quenching Of Steel Plates*", Metals Technology 7.1 (1980): 203-211.
29. Genta, G., "*Kinetic Energy Storage*", London: Butterworths, 1985.
30. Mazi`ere, M., Besson, J., Forest, S., Tanguy, B., Chalons, H., and Vogel, F., "*Overspeed Burst of Elastoviscoplastic Rotating Disks - Part 2: Burst of a Superalloy Turbine Disk*", European Journal of Mechanics - A/Solids, 28(3):428 – 432, 2009.
31. Bhaumik, S., Bhaskaran, T., Rangaraju, R., Venkataswamy, M., Parameswara, M., and Krishnan, R., "*Failure of Turbine Rotor Blisk of an Aircraft Engine*", Engineering Failure Analysis, 9(3):287 – 301, 2002.
32. Bert, C. W. and Paul, T. K., "*Failure Analysis of Rotating Disks*", International Journal of Solids and Structures', 32(89):1307 – 1318, 1995.
33. Shikida, M., Kanayama, Y., and Ohnami, M., "*A Study on High-Speed Disk Bursting Strength*", Bulletin of JSME, 23(181):1035–1042, 1980.
34. Chianese, S., "*Safety Factor Against Burst Speed Of Turbomachinery Rotating Disks*", Master Thesis, the Graduate College of the University of Illinois at Chicago, 2013.
35. Hutchinson, J. W., "*Singular Behavior at the End of a Tensile Crack Tip in a Hardening Material*", Journal of the Mechanics and Physics of Solids, Vol. 16, 1968, pp. 13-31.
36. Pruitt, L., "*Deformation, Yielding, Fracture and Fatigue Behavior of Conventional and Highly Cross-Linked Ultra High Molecular Weight Polyethylene*", Biomaterials', 26 (8), pp. 905 – 915, 2005.
37. Pelloux, R.M.N., "*Mechanisms of Formation of Ductile Fatigue Striations*", Transactions of ASM 62, 281–285, 1969.
38. Neumann, P., "*Coarse Slip Model in Fatigue*", Acta Metallurgica 17, 1219–1225, 1969.
39. Ritchie, R.O., "*Mechanisms of Fatigue-Crack Propagation in Ductile And Brittle Solids*", International Journal of Fracture 100 (1999): 55-83.
40. Young, C. W., "*The Development of Empirical Equations for Predicting Depth of an Earth Penetrating Projectile*", SC-DR-67-60. Albuquerque NM: Sandia National Laboratories, Albuquerque, NM, May 1967.
41. Bernard, R.S. and Hangud, S.V., "*Development of a Projectile Penetration Theory, Report 1, Penetration Theory for Shallow to Moderate Depths*". U.S. Army Engineers Waterways Experiment Station Technical Report 5-75-9, 1975.

42. Forrestal, M. J., Altman, B. S., Cargile, J. D., and Hanchak S. J., "*An Empirical Equation for Penetration Depth of Ogive-Nose Projectiles into Concrete Targets*", Proceedings of the Sixth international Symposium on Interaction of Nonnuclear Munitions with Structures, pp. 9-32. Panama City Beach, FL, May 3-7, 1993.
43. Young, C. W., "*Depth Predictions for Earth Penetrating Projectiles",* Journal of Soil Mechanics and Foundations SM3, May 1969.
44. Young, C. W., "*Penetration Equations'*, Sandia National Laboratories", Contractor Report: SAND 97-2426, UC-705, 1997.
45. Richmond, P.W., "*Influence of Nose Shape and L/D Ratio on Projectile Penetration in Frozen Soil",* Special Report 80-17, U.S. Army Cold Regions Research and Engineering Laboratory, 1980.
46. Kadoya, K., Matsunaga, N., and Nagashima, A., "*Viscosity and Thermal Conductivity of Dry Air in Gaseous Phase*", J. Phys. Chem. Ref. Data, Vol.14, No 4, 1985.
47. Zoueshtiagh, F. et al. "*Laminar-Turbulent Boundary-Layer Transition over a Rough Rotating Disk*", Physics of Fluids 15.8 (2003): 2441.
48. Imayama, S., Alfredsson P. H., and Lingwood R. J., "*An Experimental Study of Edge Effects on Rotating-Disk Transition*". J. Fluid Mech. 716 (2013): 638-657.
49. Blasius, H., "*Grenzschichten in Flüssigkeiten mit Kleiner Reibung*". Z. Math. Phys. 56: 1–37. 1908 (English translation)
50. VON KARMAN, T., "*Uber Laminare und Turbulente Reibung*". Z. Angew. Math. Mech., 1, pp. 232-252, 1921. (English translation)
51. "*Barden Super Precision Ball Bearings – Specialty Products*", The Barden Corporation, 2013.
52. Elsey, R. J., "*Outgassing of Vacuum Materials – I*", Vacuum 25.7 (1975): 299-306.
53. G Lewin, "*Fundamentals of Vacuum Science and Technology*", McGraw-Hill, New York 1965.
54. Moshey, E. A., "*A Compilation of Outgassing Data on Vacuum Materials"*, Engineering Technical Memorandum, Plasma Physics Laboratory, Princeton University, Doc NO. 82-001, 1982.